

Review

Advancements and Opportunities in Characterizing Patient-Specific Wall Shear Stress Imposed by Coronary Artery Stenting

John F. LaDisa, Jr. ^{1,2,3,4,*}, Arash Ghorbannia ² , David S. Marks ³, Peter Mason ³ and Hiromasa Otake ⁵

¹ Department of Pediatrics, Division of Cardiology, Herma Heart Institute, Children's Wisconsin and the Medical College of Wisconsin, Milwaukee, WI 53226, USA

² Department of Biomedical Engineering, The Medical College of Wisconsin and Marquette University, Milwaukee, WI 53226, USA

³ Department of Medicine, Division of Cardiovascular Medicine, Medical College of Wisconsin, Milwaukee, WI 53226, USA

⁴ Department of Physiology, Medical College of Wisconsin, Milwaukee, WI 53226, USA

⁵ Graduate School of Medicine, Kobe University, Kobe 657-8501, Japan

* Correspondence: jladisa@mcw.edu

Abstract: The success of drug-eluting stents (DES) is limited by restenosis and, to a lesser extent, late stent thrombosis. Mechanical stimuli have been implicated in these outcomes, with indices of wall shear stress (WSS) determined from computational simulations being reported most frequently. The current work summarizes state-of-the-art computational approaches applicable to patient-specific models aimed at further understanding changes in WSS indexes imposed by stent implantation. We begin with a review of best practices involved in the process and then summarize the literature related to stent-induced WSS alterations. Image-based reconstruction methods are also discussed, along with the latest generation boundary conditions that replicate cardiac physiology and downstream vasculature in the setting of coronary artery disease. The influence of existing material property data on WSS results obtained with geometries reconstructed from finite element modeling and fluid structure interaction (FSI) simulations is reviewed, along with the novel approaches being used to provide coronary artery plaque data that are currently missing from the literature. We also consider the use of machine learning tools that have the potential for impact when assessing the role of adverse stent-induced WSS in suboptimal clinical outcomes. We conclude by focusing on challenging cases that involve DES implantation, which may benefit from recent advancements in patient-specific computational modeling.

Keywords: drug-eluting stents; computational fluid dynamics; simulation; fluid structure interaction



Citation: LaDisa, J.F., Jr.; Ghorbannia, A.; Marks, D.S.; Mason, P.; Otake, H. Advancements and Opportunities in Characterizing Patient-Specific Wall Shear Stress Imposed by Coronary Artery Stenting. *Fluids* **2022**, *7*, 325. <https://doi.org/10.3390/fluids7100325>

Academic Editor: Huidan (Whitney) Yu

Received: 30 June 2022

Accepted: 5 October 2022

Published: 11 October 2022

Publisher's Note: MDPI stays neutral with regard to jurisdictional claims in published maps and institutional affiliations.



Copyright: © 2022 by the authors. Licensee MDPI, Basel, Switzerland. This article is an open access article distributed under the terms and conditions of the Creative Commons Attribution (CC BY) license (<https://creativecommons.org/licenses/by/4.0/>).

1. Background

Cardiovascular disease (CVD) remains the leading cause of mortality in the USA, with greater than 1000 daily CVD deaths and approximately 8 million procedures annually. A total of 126 million Americans (49.2% of adults) have CVD, and ~50% suffer from coronary artery disease (CAD) [1]. Bare metal (BMS) and drug-eluting stents (DES) have revolutionized CAD treatment. Stenting is now the most common method of revascularization and percutaneous coronary intervention (PCI). Despite notable advances, current DES are still limited by in-stent restenosis (ISR) and, to a lesser extent, stent thrombosis (ST). Restenosis is defined by a diameter reduction via angiography [2] or intravascular imaging modalities such as optical coherence tomography (OCT) [3] from excessive neointimal hyperplasia (NH; new tissue growth) [4]. Early DES decreased restenosis [5] relative to BMS but were prone to ST [6] as they inhibited endothelialization [7–9]. Newer DES improved the outcomes, but restenosis can still persist. Stent thrombosis is classified as early, late, and very late ST (>1 year after stenting). Early DES were associated with the increased incidence of

late ST (LST) and very late ST. Although far less common than restenosis, LST also remains a concern for its high rates of morbidity and mortality [10–14] and the potential for delayed healing long after DES implantation [15]. Despite the use of current DES, some studies have estimated annual restenosis rates to be around 5–10% of cases, while LST occurs in 0.2–1.0% of cases [16–18]. These issues are accentuated for challenging lesions [19] and may only be partially alleviated by next-generation DES as their use extends to other vessels in the body, including some areas without extensive experience [20].

The precise cause of poor clinical outcomes of DES in some patients remains unknown. Recent reports have pointed to procedural and biological contributors, with at least one recent classification system proposed to better differentiate contributors on a patient-specific basis [21]. The malapposition of stent struts is likely a contributor within the procedural aspect of the proposed scoring system cited above. Malapposition is defined as a portion of the stent present at a distance greater than the strut's thickness from the artery surface [22]. Malapposition can occur late as a result of positive vessel remodeling due to an eluted drug [23], or early as the result of local plaque burden [24]. Coronary anatomy such as bifurcation lesions can also impact the deformation and positioning of stent struts [25], leading to the unintentional underexpansion or undersizing of stents. Malapposition is a prominent contributor, and hence a marker, of LST and possibly NH [26,27].

Mechanical stimuli have also been implicated in poor clinical outcomes following DES implantation, with indices of wall shear stress (WSS) calculated from computational simulations being reported most frequently. Hence, the current review primarily focuses on indices of WSS and aspects of the patient-specific computational modeling process that can influence these indices. Distributions of WSS indices (see Section 3) are locally influenced by strut positioning after stenting and can also modulate artery response to the stent implantation process [28]. Previous studies and reviews [28–30] have suggested adverse flow patterns and that the potential for flow stagnation are accentuated in the setting of malapposed struts. Stenting has also been noted to cause endothelial denudation [31] and arterial damage as part of the process of restoring artery patency. Studies going back decades have convincingly shown how WSS indices can determine where the neointimal tissue establishes in response to localized injury [32–35]. The over-expansion of stents can therefore create the undesirable situation of more prominent arterial injury along with a greater percentage of the stented artery being exposed to adverse distributions of WSS.

WSS patterns correlate with sites of NH in BMS and can inhibit the endothelialization of stents [36], which prevents LST. In contrast to BMS, the data relating WSS to NH or LST for DES can be conflicting [23,37,38]. This observation underscores the need for additional studies that link detailed wall shear stress distributions after stenting, as can be revealed by patient-specific computational modeling, to the local arterial response. Despite advances in modeling capabilities, there is a paucity of important data upon which advanced simulation methods rely for the accurate assessment of WSS distributions imposed by stenting as well as the vascular response to it. For example, the materials often used with computational models of stents employ hyperelastic constitutive relationships from a limited range of plaques [39–41] despite the literature underscoring a need for more representative data [42–44]. Similarly, some reports have suggested that the mechanism of action for a DES may differentially impact the relationship between NH and WSS seen in BMS [23,37,38], but such hypotheses have not been conclusively studied in vivo or with newer DES.

With the above background in mind, the current work summarizes state-of-the-art computational approaches that are applicable to patient-specific models, aimed at further understanding WSS indices imposed by stent implantation. We begin with a general review of the steps involved in computational simulations and review the literature related to WSS indices that have historically been reported most commonly. Considering WSS alterations in response to stenting requires a brief summary of the reconstruction methods and the latest generation boundary conditions that replicate cardiac physiology and downstream vasculature in the setting of coronary artery disease. The roles of existing material property

data as well as of those that are currently missing from the literature are also reviewed. We also consider the use of current tools from mathematical and statistical sciences, such as machine learning, that have the potential for impact when assessing the role of WSS from stents in the clinical outcomes of restenosis and/or stent thrombosis. Lastly, we focus on clinical sequelae with particularly poor clinical outcomes after DES implantation that may benefit from advancements in patient-specific computational modeling.

2. Requirements and Best Practices

Patterns of fluid flow can be described by partial differential equations representing conservation laws for quantities that include mass and momentum [45]. Predicting the effect of such flows in biomedical applications and other disciplines that prominently study fluid flow is costly and time-consuming when the user does not employ computational techniques. Computational fluid dynamics (CFD) is one commonly used approach in the simulation of fluid that passes within or around objects. CFD solves the governing equations of fluid motion through numerical methods (as finite element or finite volume methods) and provides an estimation of the velocity vector in a discretized computational domain, which is represented by a collection of organized mesh elements. The current work focuses on blood vessels, where CFD allows the user to replace the partial differential equations with algebraic equations that can be solved numerically within the discretized computational domain (i.e., mesh) via digital computers. Commercial and open-source CFD software packages are available to facilitate the completion of these calculations. Most of these current-generation software packages have user-friendly interfaces that accept several types of medical imaging data. The pipeline for each software package then allows a user to generate hemodynamic results by leveraging the governing mathematical equations. Despite the apparent ease with which CFD simulations can seemingly be conducted, it is worth mentioning that there are several important considerations that the user should be cognizant of, as discussed in more detail below.

The general requirements related to studying blood flow alterations using CFD include the creation of a model of vessel geometry from medical imaging data. In addition, CFD requires the user to prescribe flow and/or pressure information at the entrance of the vessel. It is also necessary to prescribe the hemodynamic state beyond the outlets of the model created in order to obtain realistic results (e.g., imposing downstream resistance to obtain a physiologic range of pressure). Rheological properties, including the density and viscosity of blood, should then be assigned. The last step in the process involves using a powerful computer or a high-performance cluster of computers to solve the governing equations for fluid flow throughout the vessel geometry, which is represented as a computational mesh.

More precisely, the first step in performing CFD simulations involves the creation of a computer aided design (CAD) model within the arterial regions of interest, often from medical imaging data. For coronary arteries implanted with stents, this is typically angiography data from computed tomographic (CTA) or fluoroscopic systems. These data are readily available and provide a clear definition of anatomy. While CTA data sets are inherently volumetric, geometries for CFD modelling from fluoroscopic imaging systems are also sometimes reconstructed using two or more planes under certain assumptions, and higher resolution information from the stented region is then obtained via registration with an intravascular imaging modality, as discussed in more detail below. CFD geometries can also be created from other imaging modalities (e.g., magnetic resonance imaging). The models created can yield geometries on a patient-specific basis when it is desirable to focus on clinical questions for a specific patient [46] or for a group of patients with a similar pathology. Alternatively, idealized models are sometimes created to study blood flow that is generally reflective of a patient population. In such situations, the geometry within the model is typically informed by measurements taken from data within a collection of patients. The models may also offer guidance related to a specific clinical issue using a representative patient data set [47]. To date, our laboratory has primarily used SimVascular (simvascular.github.io), but there are other software packages that also permit the import and segmentation of

medical imaging data, including ITK-SNAP (www.itksnap.org, accessed on 29 June 2022), Cardiovascular Integrated Modeling and Simulation (CRIMSON, www.crimson.software, accessed on 29 June 2022), Vascular Modeling Toolkit (VMTK, www.vmtk.org, accessed on 29 June 2022), Mimics (www.materialise.com/en/healthcare/mimics-innovation-suite, accessed on 29 June 2022, Plymouth, MI, USA), and others. Each of these programs facilitates the discretization of a CAD model after it has been created from imaging data by interacting with some type of meshing software. The parameters selected during the segmentation and meshing steps can have a large influence on the results obtained. For example, the accuracy of WSS distributions (see below for details on specific indices of WSS) substantially depends on the artery radius. Therefore, the care and reproducibility with which segments or 3D boundaries for the CAD model are created from the available imaging data is important in resulting WSS distributions.

In its simplest form (e.g., plane Couette flow), WSS is calculated as the product of viscosity and the rate of deformation (i.e., near-wall velocity gradient; Figure 1). For CFD, this change in velocity from the wall of an artery to the next nearest location is dictated by the arrangement of elements and local details of the computational mesh that has been created. The velocity on the wall is often zero due to a no-slip condition that is applicable to the interaction between the flowing blood and the vessel. Unfortunately, the computational costs (time and compute resources) of obtaining CFD results increases as a function of mesh density. This trade-off is often balanced in CFD studies through the use of adaptive meshing approaches [48–51], which can produce greater mesh density in spatial locations where it is most needed as a result of complex flow patterns. Such locations include the area near the vessel wall where, as mentioned above, improved accuracy is important for determining indices of WSS. As alluded to above, WSS indices are calculated from the velocity field and therefore cannot be directly quantified using transducers or non-invasive approaches *in vivo*. Hence, in the setting of careful reconstruction methods and results independent of the computational mesh (see below), CFD simulations allow for the computation of hemodynamic quantities such as WSS that are clinically difficult or even impossible to assess with a high degree of accuracy.

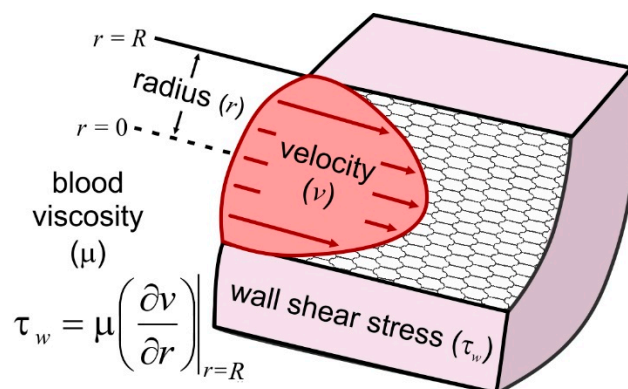


Figure 1. The figure provides an illustration of the velocity profile experienced by endothelial cells lining an artery as a result of blood flow, and a general expression for wall shear stress (τ_w ; WSS). In its simplest form, WSS can be defined as the frictional force imposed on the blood vessel wall. For this simple case, WSS is the product of viscosity (μ) and the shear rate, which is also known as the rate of deformation or near-wall velocity gradient ($\partial v/\partial r$). Adapted from Samyn and LaDisa [52].

In practice, a value for the density of blood is typically selected from the literature. A Newtonian assumption (i.e., constant blood viscosity) is also most often employed. Although blood is a shear-thinning fluid, approximating its behavior as Newtonian may be reasonable, depending on the range of shear rates experienced by the portion of the vasculature being studied and the indices being reported [53]. Newtonian and non-Newtonian (e.g., Carreau) models have been implemented [54–56], which may provide more realistic

results at certain times during the cardiac cycle and near stent struts when other sources of realism have been included and when sources of uncertainty in the modeling process have been mitigated; for example, in patient-specific simulations where reconstruction accuracy or physiologic boundary conditions have been implemented [57].

One unique aspect of CFD software programs specifically designed for blood flow in vessels lies in their ability to impose boundary conditions that replicate normal and pathologic physiology. Methods imposed for patient-specific inlet boundary conditions include velocity-encoded (VENC; i.e., phase-contrast) flow data from magnetic resonance imaging (PC-MRI). The patient-specific inlet flow rate can also be obtained from angiography [58]. When such data are not available, other approaches such as waveforms from the literature are sometimes made to approximate patient-specific conditions by scaling according to the body surface area. In terms of outlet boundary conditions, the impedance spectra (i.e., time-varying opposition to blood flow) can be determined from flow and pressure measurements if they are obtained at the same location in the vasculature. Given the impracticality of the necessary measurements within a clinical setting, Windkessel models are often used as an approximation of the impedance spectra [59] at the outlets of computational models. It is increasingly common in CFD modelling of applications involving non-coronary arteries to employ Windkessel representations derived from blood pressure measurements and PC-MRI flow data for outlet boundary conditions. The use of these more recent outlet boundary conditions is often associated with backflow stabilization methods [60,61], which limit the need for the extension of outlets, as had been commonly applied in the past. Pronounced resistance introduced by ventricular contraction results in a non-linear and time-varying system for the coronary arteries [62]. Recent advancements related to boundary conditions also account for this physiology by including the ability to mimic cardiac function through the use of closed-loop lumped-parameter networks (LPNs) with CFD models. Although initially developed to model single ventricle physiology, closed-loop LPNs are now being used to characterize flow patterns in the coronary arteries and other vascular regions [63]. The parameters used with closed-loop LPN models are typically tuned based on clinically obtained data (e.g., cardiac output, stroke volume, blood pressure, and ejection fraction). Diameter-based scaling laws have also been widely adopted in cases where the coronary branches are included, and the specific approaches implemented to date have been nicely summarized in a recent book chapter by Chiastra, Dubini, and Migliavacca [64].

As mentioned above, upon setting boundary conditions, patient-specific simulations then use specialized computers to solve for the conservation of mass and the balance of fluid momentum. In some cases, the elastodynamic equations [65] are also solved, allowing for fluid–structure interaction (FSI) simulations that replicate local deformation. FSI simulations therefore represent an extension beyond CFD modelling that considers the elastic nature and pulsatility of the arterial system. FSI modelling has the potential to introduce more clinically relevant features when determining WSS indices by including realistic local deformations. For example, when again considering the simple case of WSS calculated as the product of the near-wall velocity gradient and viscosity, the movement of the vessel wall, as it occurs *in vivo*, will impact this calculation [66]. Most coronary artery stents are relatively rigid to prevent recoil with the stented region [67], but including local deformations in WSS calculations has the potential to provide more realistic results and strains within intra-strut regions [66]. While the impact of FSI simulations on distributions of WSS in the literature has so far been dependent on available material properties, FSI studies conducted in idealized arteries with computational replicas of several commercially available stents show the advantages of circumferentially oriented sinusoidal strut patterns with limited connector elements and large open-cell designs, which have the smallest deviations in Von Mises stress and displacement when exposed to dynamic curvature [68]. Such studies provide support for design aspects that have been implemented by manufactures for decades. As with all the considerations above, adding the realism of deformable walls often leads to increased computational time. Hence, the need for this advancement should be considered relative to its importance, in relation to the quantities being reported. Con-

versely, simulating pulsatile blood flow for transient portions of the vasculature such as the coronary arteries, and best practices such as mesh independence, the presentation of results that are independent of the time step employed during a simulation, and the assurance that the results are periodic all represent considerations that are usually important regardless of the indices being studied.

3. Intravascular Reconstruction for Computational Simulations

Given the importance of geometry in the simulation process and WSS calculations reviewed above, it is not surprising that multiple approaches have been developed for the reconstruction of coronary arteries used in computational simulations [69–73], many of which using OCT data have recently been reviewed by Chiastra et al. [74]. We previously developed methods [73] to create patient-specific coronary artery reconstructions by combining conventional extravascular and high-resolution intravascular imaging. Our work in this area has featured the fusion of CTA with OCT data, but the conventional imaging data source could also be MRI or biplane angiography. Biplane (i.e., orthogonal) angiographic images are often used to determine the intravascular imaging pathway and have also been used to reconstruct a vessel lumen. Although biplane angiography is a common clinical process that is performed during PCI, non-orthogonal views, differences in data acquisition between planes, movement resulting from cardiac and/or respiratory dynamics, visibility of the imaging device, and general image quality are potential issues that may arise with this approach. Our approach (Figure 2) uses the conventional extravascular imaging data to establish boundaries for an optimization routine that determines the mathematical location of the intravascular imaging wire during pullback. The intravascular images provide high-resolution information from within the stented region, thereby theoretically permitting the use of volumes generated from biplane imaging planes despite the limitations mentioned above. Besides OCT, the high-resolution data can also come from IVUS. Both modalities can capture stent linkages. OCT has 10x the resolution of IVUS but requires contrast, and therefore some interventional cardiologists prefer IVUS. Our reconstruction and stenting approaches work with data from either modality. Briefly, intravascular images are processed to isolate lumen versus stent contours (i.e., segments) by thresholding. The pathway traversed by the wire during pullback is calculated by minimizing the total bending energy [73] within the volume delineated by the extravascular imaging data. Lumen segments are then registered longitudinally on the wire pathway using landmarks and according to the intravascular image spacing. These lumen segments are oriented such that they are orthogonal to the wire pathway and rotated so that the centroids are aligned with the vessel centerline. The aligned and oriented segments are then loaded into SimVascular for lofting and blending. The implanted DES from post-stenting OCT or IVUS is quickly replicated in reconstructions by a series of Boolean operations [66,73] or structural finite element modeling (FEM) [46]. Similar to full-scale structural FEM simulations that include stent recoil, the series of Boolean operations implemented for this approach can capture local stent malapposition.

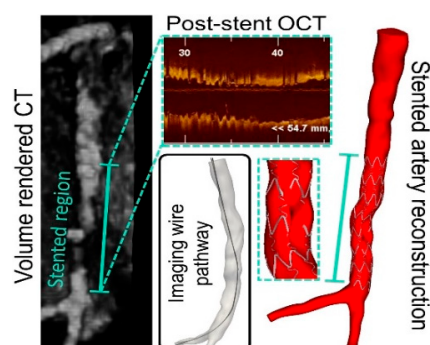


Figure 2. One method of patient-specific stented artery reconstruction. A coronary CTA is seeded with candidate points, and the OCT imaging wire path is calculated by minimizing total bending energy. The implanted stent is then replicated computationally. Adapted from Ellwein et al. [73].

Wu et al. recently created a reconstruction approach that is specifically tailored to coronary bifurcations [69]. Reproducibility and accuracy were assessed in five silicone bifurcation models created from patient-specific angiography, which then underwent OCT imaging and were compared to reference versions from contrast-enhanced microfocal computed tomography (μ CT). The utility of the method was further scrutinized in seven diseased patient bifurcations of varying anatomical complexity. Agreement was high between reconstructions and reference morphology, as was reproducibility and the ability to conduct the reconstruction process within a reasonable amount of time (i.e., <1 h). This method has since been extended, with angiography and OCT data obtained directly from patients and with the addition of local linkages resulting from deployment through the optimization of several bifurcation stenting techniques [75].

Other approaches in the combination of conventional extravascular and high-resolution intravascular imaging data to reconstruct the stented flow domain are also presented with varying degrees of detail in the literature [70,76–79]. Recently, Li and colleagues described their process using 3D angiography and OCT imaging, which was featured for diseased coronary artery data sets [80] as well as those obtained after bioresorbable vascular scaffold (BVS) implantation [58]. Their approach pays particular attention to the inclusion of side branches that are likely to impact the local flow field. A similar approach was employed for BVS by Migliori et al., who further quantified restenosis and neointimal thickening [76]. Gogas et al. developed a similar process that is highlighted via a BVS case study [77,78]. Their approach is noted for including semiautomated lumen extraction and strut detection via shape recognition algorithms within each OCT image. These data are then aligned while accounting for patient curvature.

The choice of which intravascular imaging modality is to be used in each approach (e.g., OCT vs. IVUS) depends on many factors, such as those present from a clinical perspective that are related to the need for contrast, onboard versus offline plaque characterization protocols as well as clinical preference and the availability of each clinical imaging system within a given catheterization laboratory. While acknowledging these considerations, studies have suggested that patient-specific arteries created from OCT and IVUS runs of the same atherosclerotic arteries may be highly correlated [81]. In contrast, when conducted after stenting, it appears that there can be significant differences in clinical endpoints such as the thickness and area of neointimal tissue that impact local blood flow patterns manifesting in the WSS imposed on the endothelium [82]. These differences seem to be a result of improved resolution afforded by OCT.

It is important to note that to date, the inclusion of stents in computational models of reconstructed arteries has ranged from the general contour traced out by stent struts in intravascular images while ignoring the local struts and their associated perturbations, to the incorporation of residual stresses and strains experienced during balloon folding and pleating and stent crimping. Particularly noteworthy is the work of Chiastra et al., which demonstrated the importance of including local stent struts in patient-specific reconstructions exposed to steady inflow boundary conditions [55]. Local distributions of TAWSS are drastically different due to the geometry of the implanted stent, with 35% of the modelled left anterior descending coronary artery exposed to adverse TAWSS (i.e., <4 dyn/cm²) for the stented case; this was only 2.6% when local struts and their perturbations were ignored [64]. The inclusion of residual stresses and strains experienced during balloon folding and pleating and stent crimping was shown to significantly increase the accuracy of deformations obtained from stent deployment simulations [83]. Although the authors used a 316 L stainless steel stent when many current stents are made of cobalt chromium, their point is well-taken and interesting for several reasons. First, the detailed geometry after implantation impacts the local flow disturbances manifested in indices of WSS and the response of the artery to DES-induced damage, but also because issues in the DES manufacturing process unique to a given DES may also influence the potential for local stent malapposition, which has been associated with LST and NH [26,27], as mentioned above.

4. WSS Findings to Date and Related Indices of Interest

Mechanical stimuli have been shown to influence the onset and progression of CVD. As alluded to above, WSS is of particular interest in response to stent implantation. In prior studies, sites of low time-averaged WSS (TAWSS) were thought to correlate with the localization of atherogenesis and inflammation [84–88]. These studies motivated the early hypotheses related to whether alterations in WSS manifesting from stenting may ultimately contribute to NH. Although WSS is represented by vectors that change instantaneously throughout the cardiac cycle, most studies report time-averaged representations along the wall for the region of interest. This is likely carried out for simplicity and because the mechanisms by which a each WSS index leads to NH are not yet fully known. There is some evidence indicating that spatial and temporal WSS alterations may also serve as stimuli for neointimal thickening. Many CFD studies also report the oscillatory shear index (OSI) [87], which is a measure of WSS directionality. Lower OSI values indicate that WSS is predominantly oriented in the primary direction of blood flow, whereas a value of 0.5 indicates bi-directional WSS with a time-averaged value of zero. Sites of the vasculature exposed to low WSS magnitude and high OSI are theoretically less likely to experience fluid forces that allow for the washout of noxious and potentially atherogenic materials in contact with the arterial surface (e.g., LDL). In general, adverse values for these indices are expressed as thresholds (e.g., TAWSS ≤ 4 dyn/cm² for the coronary arteries [86]). Data from prior idealized and preclinical stenting studies suggest that an OSI greater than ~ 0.1 may also be considered adverse [47], as well as spatial and temporal WSS gradients greater than 100 dyn/cm³ and ± 200 dyn/cm²/s, respectively [88–90].

New indices that attempt to better capture the stimuli exposed in an artery continue to be derived. One such index is the WSS exposure time (WSSET). The WSSET is determined from the vectorized form of WSS and generally represents the accumulated amount of time WSS trajectories visit a mesh element over the cardiac cycle [91]. When applied in computational simulations of DES, WSSET provides some measure of drug transport associated with each DES in the setting of local hemodynamics stimuli and its potential relationship to NH or resorption in a patient-specific manner. Additional indices of interest include helicity (sometimes reported as a normalized version that considers local velocity and vorticity magnitude) and relative residence time (RRT). Local normalized helicity describes the alignment of streamlines into spiral patterns within arteries [92]. RRT is considered an aggregate index of TAWSS and OSI, as both are included in its calculation. As its name implies, RRT is interpreted as a measure of particle residence time near the wall, with elevated RRT being linked to cellular proliferation in other vascular beds [93,94]. Results from patient-specific models exposed to steady boundary conditions have noted values for WSS and RRT that tend to be localized to regions of NH adjacent to stent struts, within bifurcations and in zones where stents are overlapping [55].

Over the past two decades, numerous studies have been conducted to determine if adverse distributions of WSS unique to the geometry of the stented portion of an artery correlate with NH. For example, we previously showed that areas of low WSS established after BMS implantation modulate the development of NH in rabbit iliac arteries [32]. As NH occurs within a stent implanted into an otherwise healthy artery, the geometry and associated WSS distributions change over time to progressively alleviate deleterious WSS distributions initially created by stenting. Additional studies by our lab and others [32,89,95–98] further demonstrated that the geometric properties of a stent may contribute to adverse indices (e.g., low TAWSS) associated with NH. Idealized studies have further shown that the number, width, and thickness of stent struts as well as the severity of shortening, local scaffolding, and the degree of curvature created by a stent can introduce potentially adverse flow disturbances that may lead to NH [32,89,97,99,100]. More specifically, the thickness and number of stent struts are believed to have a greater impact on the development of NH than their width [99]. The thickness of struts causes protrusion of the stent into the flow domain, which in turn causes disruptive flow patterns and increases in the area of the vessel exposed to adverse WSS. This theoretical finding is supported by numerous

controlled preclinical and clinical studies [31,101,102]. Similarly, by increasing the number of stent struts, a greater scaffolding of the lumen is accomplished by limiting the protrusion of the vessel wall between linkages, which then leads to increased longitudinal and circumferential uniformity within the stented region [99]. However, since all stent struts disturb blood flow, the relative ratio of the stent-to-vessel area can cause deleterious flow patterns depending on the orientation of the struts in relation to the flow direction. These findings from idealized stented models have also served as a means of understanding similar computational studies using more recent stent geometries [103,104]. While the understanding recounted above does not necessarily remain true in the setting of diseased human coronary arteries implanted with current DES, it does provide the intuition with which flow disturbances resulting from more realistic clinical scenarios can be interpreted. The effect of the stent struts on the local hemodynamics, which results in the behavior recounted above, has been previously discussed in detail [89,105] and generally involves struts redirecting local velocity vectors in a converging or diverging manner; this is based on the orientation of the struts in relation to the primary direction of the blood flow and depends on the overall geometry of the stent model. Helical flow structures can also result from any curvature upstream of the stent and in bifurcation regions [55]. Such details have since been associated with an index called the WSS topological skeleton, which is calculated from the divergence of the normalized WSS vector field and provides an additional characterization of the forces that may be experienced by cells along the stented vessel surface [106].

Recent computational studies have also provided further details on altered indices of WSS and stent thrombosis. For example, Ng et al. studied the acute impact of strut malapposition and underexpansion of stents using a 2.75 mm inner diameter isotropic benchtop silicon model with elastic material properties (density 1110 kg/m³; Young's modulus 1.2 MPa; Poisson's ratio 0.48, 0.45 mm thickness) and a 40% diameter stenosis [107]. Models implanted with fully apposed and malapposed sirolimus-eluting stents in the stenotic region were perfused with porcine blood for 1 h at 200 mL/min. The takeaway of their work was that underexpansion alone did not substantially impact thrombus formation, but thrombus assessment and quantification via OCT pullback was noted when underexpansion was co-localized with malapposition. Although malapposition in the absence of stent underexpansion was not studied, Gasior et al. conducted a related study in which a dedicated bifurcation stent was compared with other commercially available stents implanted in a bifurcation model [108]. Computational modeling with OCT and immunofluorescence following perfusion with porcine blood for the same duration and flow rate above revealed that indices of thrombus were more pronounced for stents in which malapposed struts and the associated WSS alterations were present at the side branch ostia.

When considering CFD simulations of stented human coronary arteries, the most common type of result reported to date has been the extraction of WSS distributions from steady simulations. There is merit to such studies as the vascular response to stimuli likely represents some integrated measure of exposure to mechanical stimuli over time, and it is reasonable to surmise that mean WSS provides a representative index of that exposure. However, data relating WSS to NH or LST for DES can be somewhat conflicting [23,37,38], which makes the details associated with computational modeling methods employed for a particular study important. Each study in this area has undoubtedly been useful and serves as a foundation for our understanding to date, but future work will expand on this work to include more detailed perturbations from the local contours of individual struts that impact our understanding of mean WSS as well as other indices that have recently been reported.

5. Optimizing the Stenting Procedure

The use of optimization in a mathematical sense allows for a systematic and unbiased approach to maximizing or minimizing a function relative to some design criteria. The

use of optimization in stent design and model selection for patients is intriguing, given the idealized CFD findings reviewed above. The use of optimization in CFD is not new; Marsden and colleagues applied an optimization algorithm to surgically reconstruct vessels of children with a single functioning ventricle [109], while other notable work has also been conducted [110]. However, the application of optimization theory to stenting has so far been limited. Hence, in contrast to the abovementioned patient-specific work with realistic boundary conditions, in this section, we more generally review the optimization work related to the more idealized modeling of stents that has been performed. For example, our lab applied a surrogate management framework optimization algorithm for 3D CFD of stents using idealized BMS models [111,112]. Computational approaches such as this are not routinely implemented within stent development companies, possibly since a product can often be created and tested more rapidly than a computational analysis can be conducted. However, CFD is becoming more efficient [113] and can provide insights that cannot be obtained from bench-top testing or from the evaluation of prototypes using design matrices. Since any number of permutations can be modified computationally, optimization algorithms can facilitate the evaluation of theoretical and virtual approaches that could offer distinct advantages in a systematic and unbiased manner. Findings from an initial analysis showed that an existing optimization framework could be integrated with CFD of stents to determine the optimal angle of stent struts relative to the primary flow direction [111], and a follow-up study [112] recommended modified sizing matrices relative to those used by manufacturers of common stents for 2–5 mm diameter arteries (Figure 3). A more recent work applied multi-objective optimization to 12 mm stents within idealized cylinders to identify optimal strut width, thickness, angle, longitudinal spacing, and connector shape based on the percentage of vessel area exposed to low TAWSS, high TAWSS, and radial stiffness [114]. Results were generally consistent with those previously presented and with anecdotal stent design knowledge, but they also showed important differences based on whether strut cross sections were modelled as circular or rectangular.

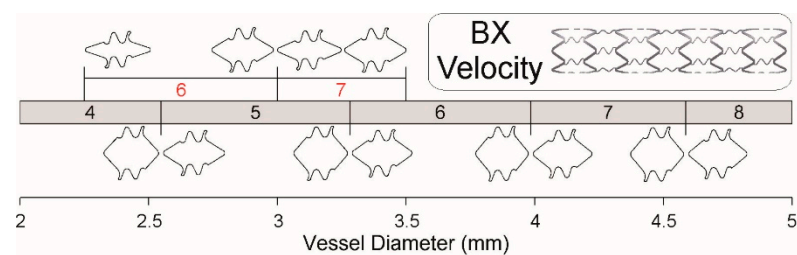


Figure 3. Comparing diameter ranges of a commercial stent vs. its diameter ranges for optimal WSS. The number of repeating units from the manufacturer’s sizing matrix is shown (red values) with that from optimization using a TAWSS cost function (black values). The geometry of one unit for the limits of each range is also shown. Adapted from Gundert et al. [112].

The study mentioned above, which showed differences in optimal strut design based on its cross-sectional shape, is interesting, particularly considering a recent work that featured a parametric level set method to optimize the topology of struts [115]. This approach allows for the systematic computational modification of structural topologies to arrive at novel strut structures that may not have previously been devised. Although in its infancy relative to other current state-of-the-art CFD stimulations of stented arteries (e.g., steady flow, zero pressure outlet boundary conditions, sheet configuration), future work aimed at applying these approaches to patient-specific stent designs is exciting, given the existence of 3D printing/additive manufacturing techniques as well as current abilities to modify strut shapes through processes including wire electrical discharge machining.

Bench top studies from over a decade ago showed that the angle and orientation of stent struts can impact the potential for endothelialization [36]. More recent studies using intravascular imaging modalities have shown that stent malapposition can be associated with delayed neointimal healing via incomplete endothelialization. Malapposition also

induces local disruptions in WSS indices that have previously been linked to neointimal proliferation and thrombus deposition in preclinical models as well as to clinical restenosis and stent thrombosis [116]. Hence, some subsequent studies have emerged to limit the likelihood of malapposition while also optimizing vessel wall stress (fluid and solid mechanics) and drug diffusion using surrogate modeling [117]. For example, by using constitutive parameters for a soft plaque [118] generally aimed at representing the combination of native vessel and plaque components [119], Ragkousis et al. were able to show [117] that the optimal deployment could be predicted computationally. Perhaps not surprisingly, malapposition was inversely proportional to stresses imposed on vascular tissue and the resulting drug diffusion, pointing to a delicate balance between implantation to optimize DES features upon delivery and local injury [120], which may adversely influence outcomes.

6. Limited Data from Atherosclerotic Arteries

There is some evidence in the literature to suggest that FSI simulations involving stents may not be necessary due to the rigidity imparted by many coronary stents on an artery [67,121]. However, the materials often used with FSI simulations involving stents as well as the flow domains obtained for CFD after the FEM of computationally deployed stents coincide with available hyperelastic constitutive relationships for a limited range of plaques [39–41] (e.g., lipid rich, fibrous, and calcified plaques [122,123]) and healthy arteries [124,125]. Our lab has also applied these methods [46], which can result in deformations with a reasonable level of agreement with reconstructed arteries. Strictly speaking, it therefore remains to be determined whether rigid wall simulations yield WSS results that are similar to FSI simulations following patient-specific assessment of local material properties. Put in another way, the utility of limited prior data falls short when the goal is to predict the likelihood of NH or LST using patient-specific computational models created with the use of imaging from the PCI period. The recent literature echoes this need for more data. Akyildiz et al. recounted how data were missing on the tensile and compressive properties of the coronary arteries because tissue was often obtained after autopsy, when mechanical properties had already degraded [42]. Chen and Kassab recently acknowledged the paucity of studies accounting for plaque substructure in constitutive models applied in coronary arteries [43]. McKittrick and colleagues further remind us that most models employed to date are from healthy vessels and do not capture the effects of disease, including the presence of atherosclerotic plaque [44]. Computational models of tissue prolapse [126] after stenting, which can impact WSS [90], have also used material properties and/or constants for their associated hyperplastic constitutive equations rooted in the references above. More clarity on material properties from a wider range of plaque types and combinations has the potential to expand prior work in order to create more accurate models of intra-strut prolapse that may be associated with restenosis on a patient-specific basis.

Recently Narayanan et al. used inverse finite element methods to estimate the material properties of arterial plaque components [127]. The authors leveraged intravascular ultrasound imaging data acquired during imaging wire pullback in vivo and an in silico (i.e., simulated) target geometry corresponding to 60 mmHg above the acquired geometry for three patients. Consistent with the work above, five material regions were identified, which included fibrous, lipid, calcium, mixed, and healthy wall tissue.

In an effort to address requests for additional material characterization studies related to atherosclerotic coronary arteries, our group has begun testing plaques obtained from fresh human coronary arteries, which were harvested after the untimely passing of patients. These arteries are obtained as part of an organ donation protocol at a partnering institution. OCT imaging was performed at 0–90 mmHg and the physiologic blood pressure noted in the associated documentation. In our initial protocol, the arteries were then dissected for uniaxial extension testing and characterized using a hyperelastic constitutive model [124]. Cauchy stress was expressed as a function of the Green–Lagrange Strain. To create a validated computational approach and to characterize plaques too small to test empirically,

inverse finite element analysis simulations were performed using the displacement from OCT at each pressure (Figure 4A). There was good agreement within the physiological range between the stress–strain curves obtained experimentally and those from inverse finite element analysis simulations (green square within Figure 4B), but there were large deviations in the super-physiological (beyond physiological) range of loading imposed during stenting (red square in Figure 4B). To mitigate this issue, biaxial material testing is now implemented to better represent in vivo loading during stenting (Figure 4C). Moreover, to translate this ex vivo loading approach beyond the physiological range to the clinic, a specialized angioplasty balloon that accommodates the OCT imaging wire has been fabricated. Deformations throughout each artery are captured via OCT at pressures according to an associated compliance table, and inverse finite element analysis simulations are again performed, yielding a constitutive characterization of the tissue across the strain range applied during PCI. Results with these methods are helping fill the void in the literature for plaque types alone and in combination, which may ultimately permit a pre-stenting plaque morphology assessment that could influence the DES choice to mitigate poor outcomes by further exploiting imaging in vivo.

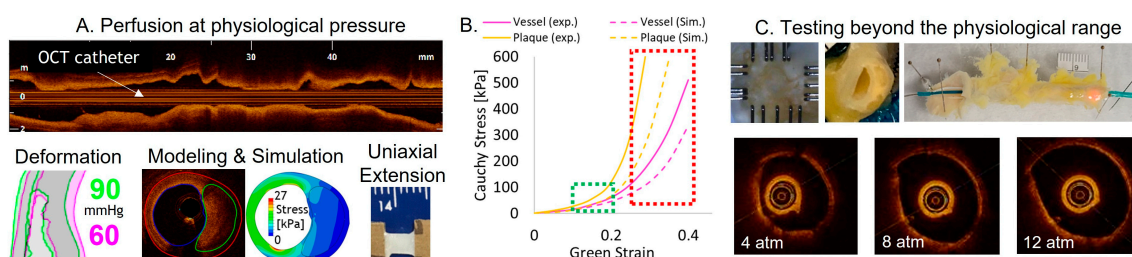


Figure 4. Current approaches to plaque characterization (A), results (B), and next-generation methods (C).

7. Application of Machine Learning (ML) and Artificial Intelligence (AI)

There is an increasing number of studies using ML and AI for several of the aspects related to the patient-specific stenting simulations reviewed above. The most common utility for such approaches seems to be the characterization of plaque components from IVUS or OCT images. As alluded to above, such advances are helpful for the field to expand beyond data currently available in the literature and to better characterize intrastent deformations as well as changes in the curvature at the proximal and distal edges of an implanted stent, which can impact WSS indices. Kolluru et al. used a decision tree classifier approach with a database of 300 images to label each voxel from OCT runs conducted with cadaver coronary arteries as fibrotic, lipid-rich, calcified, or other [128]. Bae et al. recently published their work on the use of ML approaches to predict thin-cap fibroatheroma from IVUS results co-registered in OCT images [129]. Olender et al. also presented an alternative approach and extension to the characterization afforded by virtual histology with IVUS, which characterizes plaque components into dense calcium, necrotic core, fibrotic tissue, fibro-fatty tissue, or non-pathological features [130]. Other groups have also developed automated programs that leverage ML tools to detect stent linkages in IVUS [131] or OCT [132] images, delineate stent features and vessel areas in IVUS images [133,134], as well as automatically detect bifurcations within images from an OCT run [135].

Other intriguing work in this area has been carried out by Gharleghi et al., who recently applied deep learning techniques leveraging a 2 min steady simulation, artery geometry, and global features that included radii, curvature, and bifurcation angles to obtain TAWSS distributions representative of those obtained by transient CFD simulations [136]. This example study, along with related studies that have attempted to quantify [113] and reduce the time required to obtain patient-specific simulation results, represent important advancements that are critical for CFD/FSI simulations to be able to translate from the lab to clinical utility. While the initial simulations conducted with the end goal of obtaining a

realistic patient-specific simulation and its associated WSS indices may be obtained in a ~1 day, it can easily take a month or more to tune boundary conditions, to adjust material properties until deformations are consistent with available measurements, to repeatedly quantify intermediary results, and to conduct mesh and time step independence analyses in order to generate WSS indices with a high level of confidence. It is also worth noting that although their findings were exciting and focused on the left main coronary bifurcation, Gharleghi et al. [136] and related work by Suk et al. [137] did not include stents and applied boundary conditions that were not patient-specific. Such advancements contribute substantially to the scale and complexity of the approach, thereby likely contributing the scarcity of such studies related to stenting.

Data reviewed in the Background section underscores the putative relationship between WSS indices and sites of restenosis after BMS implantation, while data relating such indices to outcomes for current-generation DES are still emerging. Groups have also applied ML tools to predict the likelihood of restenosis using angiographic and patient demographic data from the post-stenting period. Initial results suggest that such approaches may have improved predictive utility when considering the area under precision/recall curves relative to the existing restenosis scoring systems that used logistic regression, including Prevention of Restenosis With Tranilast and its Outcomes (PRESTO)-1, PRESTO-2, and Evaluation of Drug-Eluting Stents and Ischemic Events (EVENT) [138,139]. Interestingly, and to our knowledge, the ML classifiers tested identified features such as diabetes, multivessel disease, and post-PCI thrombolysis in myocardial infarction (PCI TIMI) flow as important features in the model, but did not consider stent-induced changes in WSS indices that can be revealed via CFD and/or FSI models.

8. Clinical Applications Using Patient-Specific Stenting

The best practices and considerations above have been implemented in several stenting studies with applications to specific clinical sequelae. One of the applications most poised for additional clinical guidance via computational modeling is the treatment of bifurcation lesions via provisional or two-stenting techniques. In particular, stenoses in the left main coronary artery (LMCA) can induce ischemia over a large fraction of the left ventricle and hence have the potential to result in substantial morbidity and/or mortality. One of the limitations to progress in this area is the fact that the PCI of LMCA lesions was considered harmful until recently (Class III in ACC/AHA guideline recommendations) and therefore often contraindicated during the clinical trials of DES [140,141]. Treatment with DES is now more reasonable with the recent lowering of the LMCA lesion classification, but without an abundance of available data for specific DES. Beyond being more limited in data and experience as compared to other coronary artery locations due to its prior classification, the LMCA has several unique considerations that also likely influence poor outcomes. Its derivation from the aorta makes it structurally unique, including a modest adventitia, a considerable smooth muscle content, and high elastic content proximally relative to distal coronary arteries [142]. The LMCA also has a larger caliber and shorter length [143], thus influencing its velocity profile and WSS relative to downstream arteries. LMCA lesions are present in 3–4% of the coronary catheterizations performed annually and often involve the LAD and/or LCX bifurcations. A wide range of bifurcation angles is also thought to contribute to flow disturbances and a high propensity for plaque in these bifurcations. Large-scale clinical trials are difficult due to the relatively low number of patients with LMCA lesions at most non-specialty centers and the vast number of DES designs now available. In contrast, patient-specific CFD and/or FSI simulations are well-suited to offer insight into the involvement of adverse blood flow disruptions without costly human trials or the potential for unfavorable clinical outcomes.

Recently, Samant et al. computationally and experimentally assessed the radial strength of the Synergy and several versions of the Megatron DES, which were specifically designed for the LMCA when deployed across a range of theoretical plaque types and four patient geometries [144]. Perhaps not surprisingly, the Megatron DES with 12 peaks

circumferentially provided the best radial strength relative to those with fewer peaks. Nonetheless, this work highlights the balance and interplay between indices from solid mechanics relative to those from the fluid mechanics-based optimization studies [111,112] reviewed above, and differences in indices from studies using idealized arteries implanted with commercial stents [104]. In a follow-up study by Chatzizisis et al. [145], the authors showed the feasibility of a pre-interventional LMCA DES implantation planning procedure, whereby patient-specific models were created for three cases before a Megatron stent was computationally inserted into the ‘optimal’ position, as determined by clinical guidance through consideration of the stent positioning, sizing (length, diameter, inflation pressures), and strategy for each patient. There was good agreement in the mean diameters within the stented region following computational DES implantation as compared to the mean diameters obtained from IVUS conducted after the replication of the pre-interventional planning steps within the catheterization laboratory. Existing material properties from the literature were applied regionally, resulting in more uniform computational displacements relative to those obtained in vivo by visual inspection. Although extensions were used at the inlet and outlet of the models for the CFD analysis and only a snapshot of WSS results were presented, the work presents an undoubtedly exciting glimpse of what is possible through the clinical translation of computational tools.

Another recent work has also focused on bifurcations through the creation of a computational platform for patient-specific coronary bifurcation stenting [75]. As mentioned above, the methods employed most often include the assignment of material properties from available literature data of calcific, fibrous, and fibrolipid plaque components exposed to several stent platforms and techniques using one or two stents. There was good agreement along the length of the stented main vessel between the computational and clinical results for the five test cases implemented after the training cases for the platform. A visual inspection of OCT slices versus FEM results from spatially equivalent regions also showed good agreement. As pointed out by the authors, the goal was to create a framework to replicate clinical stenting steps using a trained computational stenting platform that informs the procedure conducted in the catheterization lab. Despite some limitations, the ability to conduct this work in real time and in a way that may ultimately further reduce restenosis, neoatherosclerosis, and/or LST is fascinating.

To illustrate the importance of the studies reviewed above relative to their potential for improved outcomes by optimizing the stenting procedure and the resulting stimuli for NH and/or LST, consider the examples shown in Figure 5. The examples use data from CTA and OCT imaging sessions obtained for patients with coronary artery lesions who subsequently underwent implantation with one of several DES commonly deployed within or outside the US: Xience Prime (Abbott) or Nobori (Terumo). Image-based CFD models were created, and the influence of the implanted stent on the distributions of WSS immediately after implantation were quantified. Post-stenting WSS results from the implanted stent were then also compared to those resulting from the virtual implantation of the other stent and quantified in terms of severity (i.e., total area of low WSS). When considering the stent-induced distributions of WSS for idealized representations of each stent, the CFD results suggest that the Xience Prime design, with its lower stent-to-artery area ratio and thinner struts, would be more favorable than the Nobori stent with its thick struts. However, geometric perturbations for a given patient influencing near-wall velocity patterns are superimposed on these theoretical results and can therefore factor into the observed results. While many patients likely receive what could be considered the optimal stent for their coronary artery, these examples using virtual stent implantation suggest that it is possible for some patients to benefit from the implantation of a DES other than that selected as a result of the strut thickness for the implanted stent, its amount of malapposition, and the geometric stent pattern adjacent to any malapposed regions. These findings demonstrate that geometric stent attributes, including strut thickness and stent-to-vessel area ratio alone, may not be predictive of adverse stent-induced WSS in patient-specific arteries, as had been previously thought based on results for idealized vessels. This example lends further

support to the hypothesis that a certain DES may be more beneficial for a particular patient, thereby underscoring the excitement of computational planning tools for this purpose.

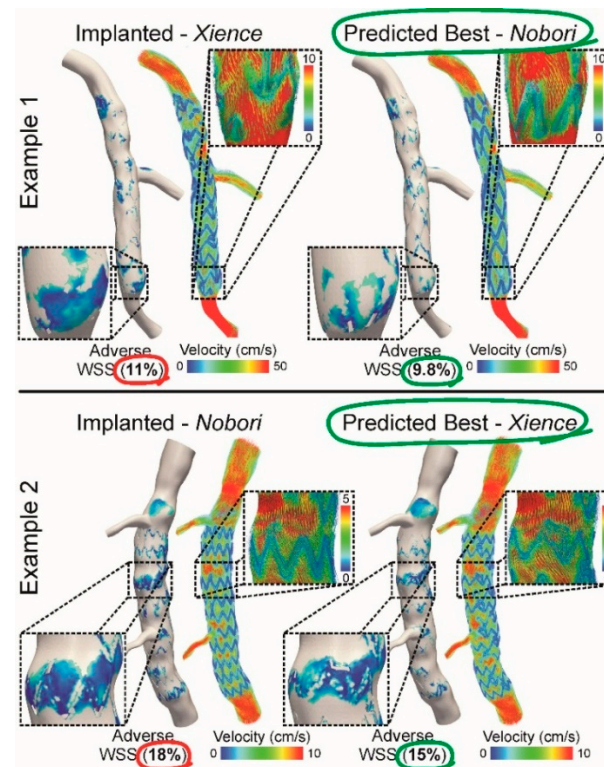


Figure 5. CFD simulations showing the amount of adverse WSS and near-wall velocity for two patients who may not have received the optimal DES according to CFD. Red circled percentages underscore more adverse areas of low WSS relative to green circled percentages for each example. These examples reveal how geometric perturbations for a given patient can factor into adverse WSS and may correlate with NH.

9. Future Directions

Among the most exciting computational advancements applicable to coronary artery disease management within the last decade is the development of a CT-derived fractional flow reserve (FFR_{ct}) index by HeartFlow [146,147]. Similar technology now also seems to be available from Toshiba [148], Siemens [149], and Canon Medical Systems Corporation. We are currently collaborating with HeartFlow for a novel research extension of their FFR_{ct} technology to noninvasively determine hemodynamically significant restenosis at follow-up, and similar approaches have been featured in at least one case report to date [150].

The ability to predict the likelihood of restenosis is intriguing, given the recent advancements in multiscale modeling [151]. For example, Zun et al. recently published an article describing a method of stent deployment and blood flow simulation, which also included tissue growth and was rooted in empirical observations of smooth muscle cell proliferation and extracellular matrix production. Their results showed good agreement with NH following BMS implantation via the use of a stent-to-artery deployment ratio of 1.4:1 in healthy curved and straight porcine coronary arteries. The adaptation of this approach in order to include the inhibitory influence of a particular DES with validation in diseased human coronary arteries subjected to clinical deployment ratios would no doubt lead to substantial excitement in the field.

Corti et al. also recently conducted an extensive review focused on the multiscale analysis of arterial adaptation in stented and unstented vessels via agent-based models [152]. In contrast to the approaches discussed above, which used continuum models based on a system of differential equations, agent-based models can provide a natural description

of biological systems using a set of rules that define agent activities such as apoptosis and mitosis [153]. This is particularly appealing when dealing with different spatiotemporal scales. Related studies to date have used such models to further elucidate the contributions of altered hemodynamics and arterial damage [154,155] in response to stenting as well as the impact of associated drugs eluted from stents to mitigate NH [156,157] and endothelialization related to LST based on WSS. Hemodynamic analyses have included idealized models (e.g., 3D with curvature) [151], and preliminary validation via histology in porcine arteries showed good agreement with model results. We eagerly await the additional extension of these approaches to patient-specific stented coronary arteries, as has been conducted in other stented vascular beds [158], which will especially contribute in an impactful way to the paucity of studies on stent thrombosis.

When considering the abovementioned details related to current technical abilities, with careful planning and in a setting with ample resources, it is possible to create truly patient-specific simulations of WSS indices today in response to an implanted DES. These models could consider local material properties extracted from pre-stent OCT conducted at multiple pressures (i.e., Figure 4C) in order to increase the likelihood of matching stent-induced deformations replicated through stent implantation via Boolean operations that leverage intravascular post-stent imaging [46] or full-scale FEM simulations of associated balloon folding, positioning, and elastoplastic expansion behavior of the stent [83]. Rheology could be included through the analysis of blood drawn from of the indwelling guide catheter, and boundary conditions that replicate the downstream pathogenic vasculature exerting pressure within the diseased coronary could be implemented using parameter estimates for coronary artery lumped parameter models [159–161]. Frequent (e.g., mean WSS) and less commonly reported stimuli (e.g., WSSET [91]) could be calculated within existing software packages or through post-processing after the convergence of simulations that consider time-step independence along with spatial mesh independence. Such simulations would be computationally expensive and time-consuming to conduct, but would provide the most comprehensive picture to date of the trade-off between the range of adverse WSS by stenting and the vascular response that is potentially mitigated by a given DES. Indeed, this is likely the future of such simulations that use current and next-generation DES as a further move toward personalized medicine, which seems to be limited only by computational ability and clinical approach. As noted above, both of these elements are rapidly progressing and becoming increasingly intertwined.

Author Contributions: Conceptualization, J.F.L.J.; investigation, J.F.L.J., A.G., D.S.M., P.M., H.O.; resources, J.F.L.J., A.G., D.S.M., P.M., H.O.; writing—original draft preparation, J.F.L.J., A.G.; writing—review and editing, J.F.L.J., A.G., D.S.M., P.M., H.O. All authors have read and agreed to the published version of the manuscript.

Funding: This research received no external funding.

Institutional Review Board Statement: Not applicable.

Informed Consent Statement: Not applicable.

Data Availability Statement: Not applicable.

Conflicts of Interest: The authors declare no conflict of interest.

References

1. Tsao, C.W.; Aday, A.W.; Almarzooq, Z.I.; Alonso, A.; Beaton, A.Z.; Bittencourt, M.S.; Boehme, A.K.; Buxton, A.E.; Carson, A.P.; Commodore-Mensah, Y.; et al. Heart Disease and Stroke Statistics-2022 Update: A Report From the American Heart Association. *Circulation* **2022**, *145*, e153–e639. [[CrossRef](#)]
2. Navarese, E.P.; Austin, D.; Gurbel, P.A.; Andreotti, F.; Tantry, U.; James, S.; Buffon, A.; Kozinski, M.; Obonska, K.; Bliden, K.; et al. Drug-coated balloons in treatment of in-stent restenosis: A meta-analysis of randomised controlled trials. *Clin. Res. Cardiol.* **2013**, *102*, 279–287. [[CrossRef](#)]
3. Lee, S.J.; Kim, B.K.; Kim, J.S.; Ko, Y.G.; Choi, D.; Jang, Y.; Hong, M.K. Evaluation of neointimal morphology of lesions with or without in-stent restenosis: An optical coherence tomography study. *Clin. Cardiol.* **2011**, *34*, 633–639. [[CrossRef](#)]

4. Hoffmann, R.; Mintz, G.S.; Dussallant, G.R.; Popma, J.J.; Pichard, A.D.; Satler, L.F.; Kent, K.M.; Griffin, J.; Leon, M.B. Patterns and mechanisms of in-stent restenosis. A serial intravascular ultrasound study. *Circulation* **1996**, *94*, 1247–1254. [[CrossRef](#)] [[PubMed](#)]
5. Krone, R.J.; Rao, S.V.; Dai, D.; Anderson, H.V.; Peterson, E.D.; Brown, M.A.; Brindis, R.G.; Klein, L.W.; Shaw, R.E.; Weintraub, W.S. Acceptance, panic, and partial recovery the pattern of usage of drug-eluting stents after introduction in the, U.S. (a report from the American College of Cardiology/National Cardiovascular Data Registry). *JACC Cardiovasc. Interv.* **2010**, *3*, 902–910. [[CrossRef](#)] [[PubMed](#)]
6. Holmes, D.R., Jr.; Kereiakes, D.J.; Garg, S.; Serruys, P.W.; Dehmer, G.J.; Ellis, S.G.; Williams, D.O.; Kimura, T.; Moliterno, D.J. Stent thrombosis. *J. Am. Coll. Cardiol.* **2010**, *56*, 1357–1365. [[CrossRef](#)]
7. Finn, A.V.; Nakazawa, G.; Joner, M.; Kolodgie, F.D.; Mont, E.K.; Gold, H.K.; Virmani, R. Vascular responses to drug eluting stents: Importance of delayed healing. *Arterioscler. Thromb. Vasc. Biol.* **2007**, *27*, 1500–1510. [[CrossRef](#)]
8. Joner, M.; Finn, A.V.; Farb, A.; Mont, E.K.; Kolodgie, F.D.; Ladich, E.; Kutys, R.; Skorija, K.; Gold, H.K.; Virmani, R. Pathology of drug-eluting stents in humans: Delayed healing and late thrombotic risk. *J. Am. Coll. Cardiol.* **2006**, *48*, 193–202. [[CrossRef](#)]
9. Kotani, J.; Awata, M.; Nanto, S.; Uematsu, M.; Oshima, F.; Minamiguchi, H.; Mintz, G.S.; Nagata, S. Incomplete neointimal coverage of sirolimus-eluting stents: Angioscopic findings. *J. Am. Coll. Cardiol.* **2006**, *47*, 2108–2111. [[CrossRef](#)] [[PubMed](#)]
10. Kimura, T.; Morimoto, T.; Kozuma, K.; Honda, Y.; Kume, T.; Aizawa, T.; Mitsudo, K.; Miyazaki, S.; Yamaguchi, T.; Hiyoshi, E.; et al. Comparisons of baseline demographics, clinical presentation, and long-term outcome among patients with early, late, and very late stent thrombosis of sirolimus-eluting stents: Observations from the Registry of Stent Thrombosis for Review and Reevaluation (RESTART). *Circulation* **2010**, *122*, 52–61.
11. Ong, A.T.; Hoye, A.; Aoki, J.; van Mieghem, C.A.; Rodriguez Granillo, G.A.; Sonnenschein, K.; Regar, E.; McFadden, E.P.; Sianos, G.; van der Giessen, W.J.; et al. Thirty-day incidence and six-month clinical outcome of thrombotic stent occlusion after bare-metal, sirolimus, or paclitaxel stent implantation. *J. Am. Coll. Cardiol.* **2005**, *45*, 947–953. [[CrossRef](#)] [[PubMed](#)]
12. Van Werkum, J.W.; Heestermaas, A.A.; de Korte, F.I.; Kelder, J.C.; Suttorp, M.J.; Rensing, B.J.; Zwart, B.; Brueren, B.R.; Koolen, J.J.; Dambrink, J.H.; et al. Long-term clinical outcome after a first angiographically confirmed coronary stent thrombosis: An analysis of 431 cases. *Circulation* **2009**, *119*, 828–834. [[CrossRef](#)]
13. Yeo, K.K.; Mahmud, E.; Armstrong, E.J.; Bennett, W.E.; Shunk, K.A.; MacGregor, J.S.; Li, Z.; Low, R.I.; Rogers, J.H. Contemporary clinical characteristics, treatment, and outcomes of angiographically confirmed coronary stent thrombosis: Results from a multicenter California registry. *Catheter. Cardiovasc. Interventions Off. J. Soc. Cardiac Angiogr. Interv.* **2012**, *79*, 550–556. [[CrossRef](#)] [[PubMed](#)]
14. Chechi, T.; Vecchio, S.; Vittori, G.; Giuliani, G.; Lilli, A.; Spaziani, G.; Consoli, L.; Baldereschi, G.; Biondi-Zoccai, G.G.; Sheiban, I.; et al. ST-segment elevation myocardial infarction due to early and late stent thrombosis a new group of high-risk patients. *J. Am. Coll. Cardiol.* **2008**, *51*, 2396–2402. [[CrossRef](#)] [[PubMed](#)]
15. De Cock, D.; Bennett, J.; Ughi, G.J.; Dubois, C.; Sinnaeve, P.; Dhooze, J.; Desmet, W.; Belmans, A.; Adriaenssens, T. Healing course of acute vessel wall injury after drug-eluting stent implantation assessed by optical coherence tomography. *Eur. Heart J. Cardiovasc. Imaging* **2014**, *15*, 800–809. [[CrossRef](#)]
16. Garg S and Serruys, P.W. Coronary stents: Current status. *J. Am. College Cardiol.* **2010**, *56*, S1–S42. [[CrossRef](#)]
17. Bonaa, K.H.; Mannsverk, J.; Wiseth, R.; Aaberge, L.; Myreng, Y.; Nygard, O.; Nilsen, D.W.; Klow, N.E.; Uchto, M.; Trovik, T.; et al. Drug-Eluting or Bare-Metal Stents for Coronary Artery Disease. *N. Engl. J. Med.* **2016**, *375*, 1242–1252. [[CrossRef](#)]
18. Byrne, R.A.; Joner, M.; Kastrati, A. Stent thrombosis and restenosis: What have we learned and where are we going? The Andreas Grüntzig Lecture ESC 2014. *Eur. Heart J.* **2015**, *36*, 3320–3331. [[CrossRef](#)]
19. Ragosta, M.; Dee, S.; Sarembock, I.J.; Lipson, L.C.; Gimple, L.W.; Powers, E.R. Prevalence of unfavorable angiographic characteristics for percutaneous intervention in patients with unprotected left main coronary artery disease. *Catheter. Cardiovasc. Interv.* **2006**, *68*, 357–362. [[CrossRef](#)]
20. Seyahi, N.; Altıparmak, M.R.; Tascilar, K.; Pekpak, M.; Serdengeçti, K.; Ereğ, E. Ultrasonographic maturation of native arteriovenous fistulae: A follow-up study. *Ren. Fail.* **2007**, *29*, 481–486. [[CrossRef](#)]
21. Shlofmitz, E.; Iantorno, M.; Waksman, R. Restenosis of Drug-Eluting Stents: A New Classification System Based on Disease Mechanism to Guide Treatment and State-of-the-Art Review. *Circ. Cardiovasc. Interv.* **2019**, *12*, e007023, reprinted in *Circ. Cardiovasc. Interv.* **2019**, *12*, e000044. [[CrossRef](#)] [[PubMed](#)]
22. Nakagawa, M.; Otake, H.; Shinke, T.; Takaya, T.; Kozuki, A.; Hariki, H.; Inoue, T.; Osue, T.; Taniguchi, Y.; Iwasaki, M.; et al. Analysis by Optical Coherence Tomography of Long-term Arterial Healing After Implantation of Different Types of Stents. *Can. J. Cardiol.* **2014**, *30*, 904–911. [[CrossRef](#)] [[PubMed](#)]
23. Gijzen, F.J.; Oortman, R.M.; Wentzel, J.J.; Schuurbiens, J.C.; Tanabe, K.; Degertekin, M.; Ligthart, J.M.; Thury, A.; de Feyter, P.J.; Serruys, P.W.; et al. Usefulness of shear stress pattern in predicting neointima distribution in sirolimus-eluting stents in coronary arteries. *Am. J. Cardiol.* **2003**, *92*, 1325–1328. [[CrossRef](#)]
24. Celi, S.; Vaghetti, M.; Palmieri, C.; Berti, S. Superficial coronary calcium analysis by OCT: Looking forward an imaging algorithm for an automatic 3D quantification. *Int. J. Cardiol.* **2013**, *168*, 2958–2960. [[CrossRef](#)] [[PubMed](#)]
25. Mortier, P.; De Beule, M.; Dubini, G.; Hikichi, Y.; Murasato, Y.; Ormiston, J.A. Coronary bifurcation stenting: Insights from in vitro and virtual bench testing. *EuroIntervention* **2010**, *6*, 53–60. [[CrossRef](#)] [[PubMed](#)]

26. Moussa, I.; Di Mario, C.; Reimers, B.; Akiyama, T.; Tobis, J.; Colombo, A. Subacute stent thrombosis in the era of intravascular ultrasound-guided coronary stenting without anticoagulation: Frequency, predictors and clinical outcome. *J. Am. Coll. Cardiol.* **1997**, *29*, 6–12. [[CrossRef](#)]
27. Kuntz, R.E.; Safian, R.D.; Carrozza, J.P.; Fishman, R.F.; Mansour, M.; Baim, D.S. The importance of acute luminal diameter in determining restenosis after coronary atherectomy or stenting. *Circulation* **1992**, *86*, 1827–1835. [[CrossRef](#)]
28. Ng, J.; Bourantas, C.V.; Torii, R.; Ang, H.Y.; Tenekecioglu, E.; Serruys, P.W.; Foin, N. Local Hemodynamic Forces After Stenting: Implications on Restenosis and Thrombosis. *Arterioscler. Thromb. Vasc. Biol.* **2017**, *37*, 2231–2242. [[CrossRef](#)]
29. De Santis, G.; Conti, M.; Trachet, B.; De Schryver, T.; De Beule, M.; Degroote, J.; Vierendeels, J.; Auricchio, F.; Segers, P.; Verdonck, P.; et al. Haemodynamic impact of stent-vessel (mal)apposition following carotid artery stenting: Mind the gaps! *Comput. Methods Biomech. Biomed. Engin.* **2013**, *16*, 648–659. [[CrossRef](#)]
30. Rikhtegar, F.; Pacheco, F.; Wyss, C.; Stok, K.S.; Ge, H.; Choo, R.J.; Ferrari, A.; Poulikakos, D.; Muller, R.; Kurtcuoglu, V. Compound ex vivo and in silico method for hemodynamic analysis of stented arteries. *PLoS ONE* **2013**, *8*, e58147. [[CrossRef](#)]
31. Garasic, J.M.; Edelman, E.R.; Squire, J.C.; Seifert, P.; Williams, M.S.; Rogers, C. Stent and artery geometry determine intimal thickening independent of arterial injury. *Circulation* **2000**, *101*, 812–818. [[CrossRef](#)] [[PubMed](#)]
32. LaDisa, J.F., Jr.; Olson, L.E.; Molthen, R.C.; Hettrick, D.A.; Pratt, P.F.; Hardel, M.D.; Kersten, J.R.; Warltier, D.C.; Pagel, P.S. Alterations in wall shear stress predict sites of neointimal hyperplasia after stent implantation in rabbit iliac arteries. *Am. J. Physiol. Heart Circ. Physiol.* **2005**, *288*, H2465–H2475. [[CrossRef](#)]
33. Liu, S.Q.; Goldman, J. Role of blood shear stress in the regulation of vascular smooth muscle cell migration. *IEEE Trans. Biomed. Eng.* **2001**, *48*, 474–483. [[CrossRef](#)]
34. Liu, S.Q.; Tang, D.; Tische, C.; Alkema, P.K. Pattern formation of vascular smooth muscle cells subjected to nonuniform fluid shear stress: Mediation by the gradient of cell density. *Am. J. Physiol.* **2003**, *285*, H1072–H1080.
35. Liu, S.Q.; Zhong, L.; Goldman, J. Control of the shape of a thrombus-neointima-like structure by blood shear stress. *J. Biomech. Eng.* **2002**, *124*, 30–36. [[CrossRef](#)] [[PubMed](#)]
36. Hamuro, M.; Palmaz, J.C.; Sprague, E.A.; Fuss, C.; Luo, J. Influence of stent edge angle on endothelialization in an in vitro model. *J. Vascular Interv. Radiol.* **2001**, *12*, 607–611. [[CrossRef](#)]
37. Papafaklis, M.I.; Bourantas, C.V.; Theodorakis, P.E.; Katsouras, C.S.; Naka, K.K.; Fotiadis, D.I.; Michalis, L.K. The effect of shear stress on neointimal response following sirolimus- and paclitaxel-eluting stent implantation compared with bare-metal stents in humans. *JACC Cardiovasc. Interv.* **2010**, *3*, 1181–1189. [[CrossRef](#)]
38. Suzuki, N.; Nanda, H.; Angiolillo, D.J.; Bezerra, H.; Sabate, M.; Jimenez-Quevedo, P.; Alfonso, F.; Macaya, C.; Bass, T.A.; Illegbusi, O.J.; et al. Assessment of potential relationship between wall shear stress and arterial wall response after bare metal stent and sirolimus-eluting stent implantation in patients with diabetes mellitus. *Int. J. Cardiovasc. Imaging* **2008**, *24*, 357–364. [[CrossRef](#)]
39. Lee, R.T.; Grodzinsky, A.J.; Frank, E.H.; Kamm, R.D.; Schoen, F.J. Structure-dependent dynamic mechanical behavior of fibrous caps from human atherosclerotic plaques. *Circulation* **1991**, *83*, 1764–1770. [[CrossRef](#)]
40. Loree, H.M.; Grodzinsky, A.J.; Park, S.Y.; Gibson, L.J.; Lee, R.T. Static circumferential tangential modulus of human atherosclerotic tissue. *J. Biomech.* **1994**, *27*, 195–204. [[CrossRef](#)]
41. Kragel, A.H.; Reddy, S.G.; Wittes, J.T.; Roberts, W.C. Morphometric analysis of the composition of atherosclerotic plaques in the four major epicardial coronary arteries in acute myocardial infarction and in sudden coronary death. *Circulation* **1989**, *80*, 1747–1756. [[CrossRef](#)] [[PubMed](#)]
42. Akyildiz, A.C.; Speelman, L.; Gijzen, F.J. Mechanical properties of human atherosclerotic intima tissue. *J. Biomech.* **2014**, *47*, 773–783. [[CrossRef](#)] [[PubMed](#)]
43. Chen H and Kassab, G.S. Microstructure-based biomechanics of coronary arteries in health and disease. *J. Biomech.* **2016**, *49*, 2548–2559. [[CrossRef](#)]
44. McKittrick, C.M.; Kennedy, S.; Oldroyd, K.G.; McGinty, S.; McCormick, C. Modelling the Impact of Atherosclerosis on Drug Release and Distribution from Coronary Stents. *Ann. Biomed. Eng.* **2016**, *44*, 477–487. [[CrossRef](#)] [[PubMed](#)]
45. De Nevers, N. *Fluid Mechanics for Chemical Engineers*, 3rd ed.; McGraw Hill: New York, NY, USA, 2004.
46. Chiastra, C.; Wu, W.; Dickerhoff, B.; Aleiou, A.; Dubini, G.; Otake, H.; Migliavacca, F.; LaDisa, J.F., Jr. Computational replication of the patient-specific stenting procedure for coronary artery bifurcations: From OCT and CT imaging to structural and hemodynamics analyses. *J. Biomech.* **2016**, *49*, 2102–2111. [[CrossRef](#)] [[PubMed](#)]
47. Williams, A.R.; Koo, B.K.; Gundert, T.J.; Fitzgerald, P.J.; LaDisa, J.F., Jr. Local hemodynamic changes caused by main branch stent implantation and subsequent virtual side branch balloon angioplasty in a representative coronary bifurcation. *J. Appl. Physiol.* **2010**, *109*, 532–540. [[CrossRef](#)]
48. Muller, J.; Sahni, O.; Li, X.; Jansen, K.E.; Shephard, M.S.; Taylor, C.A. Anisotropic adaptive finite element method for modelling blood flow. *Comput. Methods Biomech. Biomed. Eng.* **2005**, *8*, 295–305. [[CrossRef](#)]
49. Sahni, O.; Muller, J.; Jansen, K.E.; Shephard, M.S.; Taylor, C.A. Efficient anisotropic adaptive discretization of the cardiovascular system. *Comput. Methods Appl. Mech. Eng.* **2006**, *195*, 5634–5655. [[CrossRef](#)]
50. Ellwein, L.; Samyn, M.M.; Danduran, M.; Schindler-Ivens, S.; Liebham, S.; LaDisa, J.F., Jr. Toward translating near-infrared spectroscopy oxygen saturation data for the non-invasive prediction of spatial and temporal hemodynamics during exercise. *Biomech. Modeling Mechanobiol.* **2017**, *16*, 75–96. [[CrossRef](#)]

51. Kwon, S.; Feinstein, J.A.; Dholakia, R.J.; LaDisa, J.F., Jr. Quantification of local hemodynamic alterations caused by virtual implantation of three commercially available stents for the treatment of aortic coarctation. *Pediatric Cardiol.* **2014**, *35*, 732–740. [[CrossRef](#)]
52. Samyn, M.M.; LaDisa, J.F., Jr. Novel Applications of Cardiovascular Magnetic Resonance Imaging-Based Computational Fluid Dynamics Modeling in Pediatric Cardiovascular and Congenital Heart Disease. *Assess. Cell. Organ Funct. Dysfunc. Using Direct Derived MRI Methodol.* **2016**, 27–56.
53. Benard, N.; Perrault, R.; Fau-Coisne, D.; Coisne, D. Computational approach to estimating the effects of blood properties on changes in intra-stent flow. *Ann. Biomed. Eng.* **2006**, *34*, 1259–1271. [[CrossRef](#)] [[PubMed](#)]
54. Arzani, A. Accounting for residence-time in blood rheology models: Do we really need non-Newtonian blood flow modelling in large arteries? *J. R. Soc. Interface* **2018**, *15*, 20180486. [[CrossRef](#)]
55. Chiastra, C.; Morlacchi, S.; Gallo, D.; Morbiducci, U.; Cardenes, R.; Larrabide, I.; Migliavacca, F. Computational fluid dynamic simulations of image-based stented coronary bifurcation models. *J. R. Soc. Interface* **2013**, *10*, 20130193. [[CrossRef](#)] [[PubMed](#)]
56. Thondapu, V.; Tenekecioglu, E.; Poon, E.K.W.; Collet, C.; Torii, R.; Bourantas, C.V.; Chin, C.; Sotomi, Y.; Jonker, H.; Dijkstra, J.; et al. Endothelial shear stress 5 years after implantation of a coronary bioresorbable scaffold. *Eur. Heart J.* **2018**, *39*, 1602–1609. [[CrossRef](#)]
57. Lee, S.W.; Steinman, D.A. On the relative importance of rheology for image-based CFD models of the carotid bifurcation. *J. Biomech. Eng.* **2007**, *129*, 273–278. [[CrossRef](#)]
58. Li, Y.; Li, Z.; Holck, E.N.; Xu, B.; Karanasos, A.; Fei, Z.; Chang, Y.; Chu, M.; Dijkstra, J.; Christiansen, E.H.; et al. Local flow patterns after implantation of bioresorbable vascular scaffold in coronary bifurcations- novel findings by computational fluid dynamics. *Circ. J.* **2018**, *82*, 1575–1583. [[CrossRef](#)]
59. Nichols, W.W.; O'Rourke, M.F. *McDonald's Blood Flow in Arteries: Theoretical, Experimental and Clinical Principles*, 5th ed.; Hodder Arnold Group: London, UK, 2005.
60. Kim, H.J.; Figueroa, C.A.; Hughes, T.J.R.; Jansen, K.E.; Taylor, C.A. Augmented Lagrangian method for constraining the shape of velocity profiles at outlet boundaries for three-dimensional Finite Element simulations of blood flow. *Comput. Methods Appl. Mech. Eng.* **2009**, *198*, 3551–3566. [[CrossRef](#)]
61. Esmaily Moghadam, M.; Bazilevs, Y.; Hsia, T.-Y.; Vignon-Clementel, I.E.; Marsden, A.L.; Modeling of Congenital Hearts Alliance. A comparison of outlet boundary treatments for prevention of backflow divergence with relevance to blood flow simulations. *Comput. Mech.* **2011**, *48*, 277–291. [[CrossRef](#)]
62. Bovendeerd, P.H.; Borsje, P.; Arts, T.; van De Vosse, F.N. Dependence of intramyocardial pressure and coronary flow on ventricular loading and contractility: A model study. *Ann. Biomed. Eng.* **2006**, *34*, 1833–1845. [[CrossRef](#)] [[PubMed](#)]
63. Sankaran, S.; Esmaily Moghadam, M.; Kahn, A.M.; Tseng, E.E.; Guccione, J.M.; Marsden, A.L. Patient-specific multiscale modeling of blood flow for coronary artery bypass graft surgery. *Ann. Biomed. Eng.* **2012**, *40*, 2228–2242. [[CrossRef](#)] [[PubMed](#)]
64. Chiastra, C.; Dubini, G.; Migliavacca, F. Hemodynamic perturbations due to the presence of stents. In *Biomechanics of Living Organs, Biomechanics of Coronary Atherosclerotic Plaque*; Jacques Ohayon, G.F., Pettigrew, R.I., Eds.; Academic Press: Cambridge, MA, USA, 2021; pp. 251–271.
65. Figueroa, C.A.; Vignon-Clementel, I.E.; Jansen, K.E.; Hughes, T.J.R.; Taylor, C.A. A coupled momentum method for modeling blood flow in three-dimensional deformable arteries. *Comput. Methods Appl. Mech. Eng.* **2006**, *195*, 5685–5706. [[CrossRef](#)]
66. Gundert, T.J.; Shadden, S.C.; Williams, A.R.; Koo, B.K.; Feinstein, J.A.; LaDisa, J.F., Jr. A rapid and computationally inexpensive method to virtually implant current and next-generation stents into subject-specific computational fluid dynamics models. *Ann. Biomed. Eng.* **2011**, *39*, 1423–1437. [[CrossRef](#)] [[PubMed](#)]
67. LaDisa, J.F., Jr.; Hettrick, D.A.; Olson, L.E.; Guler, I.; Gross, E.R.; Kress, T.T.; Kersten, J.R.; Warltier, D.C.; Pagel, P.S. Stent implantation alters coronary artery hemodynamics and wall shear stress during maximal vasodilation. *J. Appl. Physiol.* **2002**, *93*, 1939–1946. [[CrossRef](#)]
68. Bukač, M.; Čanić, S.; Tambača, J.; Wang, Y. Fluid–structure interaction between pulsatile blood flow and a curved stented coronary artery on a beating heart: A four stent computational study. *Comput. Methods Appl. Mech. Eng.* **2019**, *350*, 679–700. [[CrossRef](#)]
69. Wu, W.; Samant, S.; de Zwart, G.; Zhao, S.; Khan, B.; Ahmad, M.; Bologna, M.; Watanabe, Y.; Murasato, Y.; Burzotta, F.; et al. 3D reconstruction of coronary artery bifurcations from coronary angiography and optical coherence tomography: Feasibility, validation, and reproducibility. *Sci. Rep.* **2020**, *10*, 18049. [[CrossRef](#)] [[PubMed](#)]
70. Slager, C.J.; Wentzel, J.J.; Schuurbijs, J.C.; Oomen, J.A.; Kloet, J.; Krams, R.; von Birgelen, C.; van der Giessen, W.J.; Serruys, P.W.; de Feyter, P.J. True 3-dimensional reconstruction of coronary arteries in patients by fusion of angiography and IVUS (ANGUS) and its quantitative validation. *Circulation* **2000**, *102*, 511–516. [[CrossRef](#)]
71. Athanasiou, L.; Nezami, F.R.; Galon, M.Z.; Lopes, A.C.; Lemos, P.A.; de la Torre Hernandez, J.M.; Ben-Assa, E.; Edelman, E.R. Optimized Computer-Aided Segmentation and Three-Dimensional Reconstruction Using Intracoronary Optical Coherence Tomography. *IEEE J. Biomed. Health Inform.* **2018**, *22*, 1168–1176. [[CrossRef](#)]
72. Timmins, L.H.; Suo, J.; Eshtehardi, P.; Molony, D.S.; McDaniel, M.C.; Oshinski, J.N.; Giddens, D.P.; Samady, H. Comparison of angiographic and IVUS derived coronary geometric reconstructions for evaluation of the association of hemodynamics with coronary artery disease progression. *Int. J. Cardiovasc. Imaging* **2016**, *32*, 1327–1336. [[CrossRef](#)]

73. Ellwein, L.M.; Otake, H.; Gundert, T.J.; Koo, B.K.; Shinke, T.; Honda, Y.; Shite, J.; LaDisa, J.F., Jr. Optical coherence tomography for patient-specific 3D artery reconstruction and evaluation of wall shear stress in a left circumflex coronary artery. *Cardiovasc. Eng. Tech.* **2011**, *2*, 212–217. [[CrossRef](#)]
74. Chiastra, C.; Migliori, S.; Burzotta, F.; Dubini, G.; Migliavacca, F. Patient-Specific Modeling of Stented Coronary Arteries Reconstructed from Optical Coherence Tomography: Towards a Widespread Clinical Use of Fluid Dynamics Analyses. *J. Cardiovasc. Transl. Res.* **2018**, *11*, 156–172. [[CrossRef](#)] [[PubMed](#)]
75. Zhao, S.; Wu, W.; Samant, S.; Khan, B.; Kassab, G.S.; Watanabe, Y.; Murasato, Y.; Sharzehee, M.; Makadia, J.; Zolty, D.; et al. Patient-specific computational simulation of coronary artery bifurcation stenting. *Sci. Rep.* **2021**, *11*, 1–17. [[CrossRef](#)]
76. Migliori, S.; Rampat, R.; Bologna, M.; Montin, E.; Burzotta, F.; Hildick-Smith, D.; Dubini, G.; Mainardi, L.; Migliavacca, F.; Cockburn, J.; et al. A Patient-Specific Study Investigating the Relation between Coronary Hemodynamics and Neo-Intimal Thickening after Bifurcation Stenting with a Polymeric Bioresorbable Scaffold. *Appl. Sci.* **2018**, *8*, 1510. [[CrossRef](#)]
77. Gogas, B.D.; Yang, B.; Piccinelli, M.; Giddens, D.P.; King, S.B., 3rd; Kereiakes, D.J.; Ellis, S.G.; Stone, G.W.; Veneziani, A.; Samady, H. Novel 3-Dimensional Vessel and Scaffold Reconstruction Methodology for the Assessment of Strut-Level Wall Shear Stress After Deployment of Bioresorbable Vascular Scaffolds From the ABSORB III Imaging Substudy. *JACC Cardiovasc. Interv.* **2016**, *9*, 501–503. [[CrossRef](#)] [[PubMed](#)]
78. Gogas, B.D.; King, S.B., 3rd; Timmins, L.H.; Passerini, T.; Piccinelli, M.; Veneziani, A.; Kim, S.; Molony, D.S.; Giddens, D.P.; Serruys, P.W.; et al. Biomechanical assessment of fully bioresorbable devices. *JACC Cardiovasc. Interv.* **2013**, *6*, 760–761. [[CrossRef](#)] [[PubMed](#)]
79. Tu, S.; Holm, N.R.; Koning, G.; Huang, Z.; Reiber, J.H. Fusion of 3D QCA and IVUS/OCT. *Int. J. Cardiovasc. Imaging.* **2011**, *27*, 197–207. [[CrossRef](#)]
80. Li, Y.; Gutierrez-Chico, J.L.; Holm, N.R.; Yang, W.; Hebsgaard, L.; Christiansen, E.H.; Maeng, M.; Lassen, J.F.; Yan, F.; Reiber, J.H.; et al. Impact of Side Branch Modeling on Computation of Endothelial Shear Stress in Coronary Artery Disease: Coronary Tree Reconstruction by Fusion of 3D Angiography and, O.C.T. *J. Am. Coll. Cardiol.* **2015**, *66*, 125–135. [[CrossRef](#)] [[PubMed](#)]
81. Papafaklis, M.I.; Bourantas, C.V.; Yonetsu, T.; Vergallo, R.; Kotsia, A.; Nakatani, S.; Lakkas, L.S.; Athanasiou, L.S.; Naka, K.K.; Fotiadis, D.I.; et al. Anatomically correct three-dimensional coronary artery reconstruction using frequency domain optical coherence tomographic and angiographic data: Head-to-head comparison with intravascular ultrasound for endothelial shear stress assessment in humans. *EuroIntervention* **2015**, *11*, 407–415. [[CrossRef](#)]
82. Bourantas, C.V.; Papafaklis, M.I.; Lakkas, L.; Sakellarios, A.; Onuma, Y.; Zhang, Y.J.; Muramatsu, T.; Diletti, R.; Bizopoulos, P.; Kalatzis, F.; et al. Fusion of optical coherence tomographic and angiographic data for more accurate evaluation of the endothelial shear stress patterns and neointimal distribution after bioresorbable scaffold implantation: Comparison with intravascular ultrasound-derived reconstructions. *Int. J. Cardiovasc. Imaging* **2014**, *30*, 485–494.
83. Geith, M.A.; Swidergal, K.; Hochholding, B.; Schratzenstaller, T.G.; Wagner, M.; Holzapfel, G.A. On the importance of modeling balloon folding, pleating, and stent crimping: An FE study comparing experimental inflation tests. *Int. J. Numer. Method Biomed. Eng.* **2019**, *35*, e3249. [[CrossRef](#)]
84. Kleinstreuer, C.; Hyun, S.; Buchanan, J.R.; Longest, P.W.; Archie, J.P.; Truskey, G.A. Hemodynamic parameters and early intimal thickening in branching blood vessels. *Crit. Rev. Biomed. Eng.* **2001**, *29*, 1–64. [[CrossRef](#)] [[PubMed](#)]
85. Ku, D.N.; Giddens, D.P.; Zarins, C.K.; Glagov, S. Pulsatile flow and atherosclerosis in the human carotid bifurcation. Positive correlation between plaque location and low oscillating shear stress. *Arteriosclerosis* **1985**, *5*, 293–302. [[CrossRef](#)]
86. Malek, A.M.; Alper, S.L.; Izumo, S. Hemodynamic shear stress and its role in atherosclerosis. *JAMA* **1999**, *282*, 2035–2042. [[CrossRef](#)]
87. Moore, J.E.; Xu, C.; Glagov, S.; Zarins, C.K.; Ku, D.N. Fluid wall shear stress measurements in a model of the human abdominal aorta: Oscillatory behavior and relationship to atherosclerosis. *Atherosclerosis* **1994**, *110*, 225–240. [[CrossRef](#)]
88. Ojha, M. Spatial and temporal variations of wall shear stress within an end-to-side arterial anastomosis model. *J. Biomech.* **1993**, *26*, 1377–1388. [[CrossRef](#)]
89. LaDisa, J.F.; Olson, L.E.; Guler, I.; Hettrick, D.A.; Kersten, J.R.; Warltier, D.C.; Pagel, P.S. Circumferential vascular deformation after stent implantation alters wall shear stress evaluated with time-dependent 3D computational fluid dynamics models. *J. Appl. Physiol.* **2005**, *98*, 947–957. [[CrossRef](#)] [[PubMed](#)]
90. White, C.R.; Haidekker, M.; Bao, X.; Frangos, J.A. Temporal gradients in shear, but not spatial gradients, stimulate endothelial cell proliferation. *Circulation* **2001**, *103*, 2508–2513. [[CrossRef](#)] [[PubMed](#)]
91. Arzani, A.; Gambaruto, A.M.; Chen, G.; Shadden, S.C. Wall shear stress exposure time: A Lagrangian measure of near-wall stagnation and concentration in cardiovascular flows. *Biomech. Modeling Mechanobiol.* **2017**, *16*, 787–803. [[CrossRef](#)] [[PubMed](#)]
92. Morbiducci, U.; Ponzini, R.; Grigioni, M.F.; Redaelli, A. Helical flow as fluid dynamic signature for atherogenesis risk in aortocoronary bypass. A numeric study. *J. Biomech.* **2007**, *40*, 519–534. [[CrossRef](#)]
93. Himburg, H.A.; Grzybowski, D.M.; Hazel, A.L.; LaMack, J.A.; Li, X.; Friedman, M.H. Spatial comparison between wall shear stress measures and porcine arterial endothelial permeability. *Am. J. Physiol. Heart Circ. Physiol.* **2004**, *286*, H1916–H1922. [[CrossRef](#)] [[PubMed](#)]
94. Hoi, Y.; Zhou, Y.; Zhang, X.; Henkelman, R.M.; Steinman, D.A. Correlation between local hemodynamics and lesion distribution in a novel aortic regurgitation murine model of atherosclerosis. *Ann. Biomed. Eng.* **2011**, *39*, 1414–1422. [[CrossRef](#)] [[PubMed](#)]

95. Bashar, A.H.; Suzuki, K.; Kazui, T.; Okada, M.Y.; Suzuki, T.; Washiyama, N.; Terada, H.; Yamashita, K. Changes in cerebrospinal fluid and blood lactate concentrations after stent-graft implantation at critical aortic segment: A preliminary study. *Interact. Cardiovasc. Thorac. Surg.* **2008**, *7*, 262–266. [[CrossRef](#)] [[PubMed](#)]
96. He, Y.; Duraiswamy, N.; Frank, A.O.; Moore, J.E., Jr. Blood flow in stented arteries: A parametric comparison of strut design patterns in three dimensions. *J. Biomech. Eng.* **2005**, *127*, 637–647. [[CrossRef](#)] [[PubMed](#)]
97. Kawaguchi, R.; Sabate, M.; Angiolillo, D.J.; Jimenez-Quevedo, P.; Suzuki, N.; Corros, C.; Futamatsu, H.; Alfonso, F.; Hernandez-Antolin, R.; Macaya, C.; et al. Angiographic and 3D intravascular ultrasound assessment of overlapping bare metal stent and three different formulations of drug-eluting stents in patients with diabetes mellitus. *Int. J. Cardiovasc. Imaging* **2008**, *24*, 125–132. [[CrossRef](#)]
98. Murphy, J.B.; Boyle, F.J. A full-range, multi-variable, CFD-based methodology to identify abnormal near-wall hemodynamics in a stented coronary artery. *Biorheology* **2010**, *47*, 117–132. [[CrossRef](#)]
99. LaDisa, J.F., Jr.; Olson, L.E.; Guler, I.; Hettrick, D.A.; Audi, S.H.; Kersten, J.R.; Warltier, D.C.; Pagel, P.S. Stent design properties and deployment ratio influence indexes of wall shear stress: A three-dimensional computational fluid dynamics investigation within a normal artery. *J. Appl. Physiol.* **2004**, *97*, 424–430. [[CrossRef](#)]
100. LaDisa, J.F., Jr.; Olson, L.E.; Hettrick, D.A.; Warltier, D.C.; Kersten, J.R.; Pagel, P.S. Axial stent strut angle influences wall shear stress after stent implantation: Analysis using 3D computational fluid dynamics models of stent foreshortening. *Biomed. Eng. Online* **2005**, *4*, 59. [[CrossRef](#)]
101. Briguori, C.; Sarais, C.; Pagnotta, P.; Liistro, F.; Montorfano, M.; Chieffo, A.; Sgura, F.; Corvaja, N.; Albiero, R.; Stankovic, G.; et al. In-stent restenosis in small coronary arteries: Impact of strut thickness. *J. Am. Coll. Cardiol.* **2002**, *40*, 403–409. [[CrossRef](#)]
102. Kastrati, A.; Mehilli, J.; Dirschinger, J.; Dotzer, F.; Schühlen, H.; Neumann, F.J.; Fleckenstein, M.; Pfaffert, C.; Seyfarth, M.; Schomig, A. Intracoronary stenting and angiographic results: Strut thickness effect on restenosis outcome (ISAR-STERO) trial. *Circulation* **2001**, *103*, 2816–2821. [[CrossRef](#)]
103. Beier, S.; Ormiston, J.; Webster, M.; Cater, J.; Norris, S.; Medrano-Gracia, P.; Young, A.; Cowan, B. Hemodynamics in Idealized Stented Coronary Arteries: Important Stent Design Considerations. *Ann. Biomed. Eng.* **2016**, *44*, 315–329. [[CrossRef](#)]
104. Gundert, T.J.; Dholakia, R.J.; McMahon, D.; LaDisa, J.F. Computational fluid dynamics evaluation of equivalency in hemodynamic alterations between Driver, Integrity, and similar stents implanted into an idealized coronary artery. *J. Med. Devices* **2013**, *7*, 011004. [[CrossRef](#)]
105. LaDisa, J.F., Jr.; Guler, I.; Olson, L.E.; Hettrick, D.A.; Kersten, J.R.; Warltier, D.C.; Pagel, P.S. Three-dimensional computational fluid dynamics modeling of alterations in coronary wall shear stress produced by stent implantation. *Ann. Biomed. Eng.* **2003**, *31*, 972–980. [[CrossRef](#)] [[PubMed](#)]
106. Chiastra, C.; Mazzi, V.; Lodi Rizzini, M.; Calo, K.; Corti, A.; Acquasanta, A.; De Nisco, G.; Belligiano, D.; Cerrato, E.; Gallo, D.; et al. Coronary Artery Stenting Affects Wall Shear Stress Topological Skeleton. *J. Biomech. Eng.* **2022**, *144*, 061002. [[CrossRef](#)] [[PubMed](#)]
107. Ng, J.C.K.; Lian, S.S.; Zhong, L.; Collet, C.; Foin, N.; Ang, H.Y. Stent malapposition generates stent thrombosis: Insights from a thrombosis model. *Int. J. Cardiol.* **2022**, *353*, 43–45. [[CrossRef](#)] [[PubMed](#)]
108. Gasior, P.; Lu, S.; Ng, C.K.J.; Toong, W.Y.D.; Wong, E.H.P.; Foin, N.; Kedhi, E.; Wojakowski, W.; Ang, H.Y. Comparison of overexpansion capabilities and thrombogenicity at the side branch ostia after implantation of four different drug eluting stents. *Sci. Rep.* **2020**, *10*, 20791. [[CrossRef](#)]
109. Katritsis, D.; Kaiktsis, L.; Chaniotis, A.; Pantos, J.; Efstathopoulos, E.P.; Marmarelis, V. Wall shear stress: Theoretical considerations and methods of measurement. *Prog. Cardiovasc. Dis.* **2007**, *49*, 307–329. [[CrossRef](#)]
110. Pizarro, C.; De Leval, M.R. Surgical variations and flow dynamics in cavopulmonary connections: A historical review. *Semin. Thorac. Cardiovasc. Surg. Pediatr. Card Surg. Annu.* **1998**, *1*, 53–60. [[CrossRef](#)]
111. Gundert, T.J.; Marsden, A.L.; Yang, W.; LaDisa, J.F., Jr. Optimization of cardiovascular stent design using computational fluid dynamics. *J. Biomech. Eng.* **2012**, *134*, 011002. [[CrossRef](#)]
112. Gundert, T.J.; Marsden, A.L.; Yang, W.; Marks, D.S.; LaDisa, J.F., Jr. Identification of hemodynamically optimal coronary stent designs based on vessel caliber. *IEEE Trans. Biomed. Eng.* **2012**, *59*, 1992–2002. [[CrossRef](#)]
113. LaDisa, J.F.; Bowers, M.; Harmann, L.; Prost, R.; Doppalapudi, A.V.; Mohyuddin, T.; Zaidat, O.; Migrino, R.Q. Time-efficient patient-specific quantification of regional carotid artery fluid dynamics and spatial correlation with plaque burden. *Med. Phys.* **2010**, *37*, 784–792. [[CrossRef](#)]
114. Gharleghi, R.; Wright, H.; Luvio, V.; Jepson, N.; Luo, Z.; Senthurnathan, A.; Babaei, B.; Prusty, B.G.; Ray, T.; Beier, S. A multi-objective optimization of stent geometries. *J. Biomech.* **2021**, *125*, 110575. [[CrossRef](#)] [[PubMed](#)]
115. Xue, H.; Saha, S.C.; Beier, S.; Jepson, N.; Luo, Z. Topological Optimization of Auxetic Coronary Stents Considering Hemodynamics. *Front. Bioeng. Biotechnol.* **2021**, *9*, 728914. [[CrossRef](#)] [[PubMed](#)]
116. Ozaki, Y.; Okumura, M.; Ismail, T.F.; Naruse, H.; Hattori, K.; Kan, S.; Ishikawa, M.; Kawai, T.; Takagi, Y.; Ishii, J.; et al. The fate of incomplete stent apposition with drug-eluting stents: An optical coherence tomography-based natural history study. *Eur. Heart J.* **2010**, *31*, 1470–1476. [[CrossRef](#)] [[PubMed](#)]
117. Ragkousis, G.E.; Curzen, N.; Bressloff, N.W. Multi-objective optimisation of stent dilation strategy in a patient-specific coronary artery via computational and surrogate modelling. *J. Biomech.* **2016**, *49*, 205–215. [[CrossRef](#)] [[PubMed](#)]

118. Ragkousis, G.E.; Curzen, N.; Bressloff, N.W. Simulation of longitudinal stent deformation in a patient-specific coronary artery. *Med. Eng. Phys.* **2014**, *36*, 467–476. [[CrossRef](#)] [[PubMed](#)]
119. Wong, H.C.; Cho, K.N.; Tang, W.C. Bending of a stented atherosclerotic artery. In *COMSOL Conference*; Comsol: Boston, MA, USA, 2009.
120. Welch, T.R.; Eberhart, R.C.; Banerjee, S.; Chuong, C.J. Mechanical Interaction of an Expanding Coiled Stent with a Plaque-Containing Arterial Wall: A Finite Element Analysis. *Cardiovasc. Eng. Technol.* **2016**, *7*, 58–68. [[CrossRef](#)]
121. Chiastra, C.; Migliavacca, F.; Martinez, M.A.; Malve, M. On the necessity of modelling fluid-structure interaction for stented coronary arteries. *J. Mech. Behav. Biomed. Mater.* **2014**, *34*, 217–230. [[CrossRef](#)]
122. Schroeder, S.; Kuettner, A.; Leitritz, M.; Janzen, J.; Kopp, A.F.; Herdeg, C.; Heuschmid, M.; Burgstahler, C.; Baumbach, A.; Wehrmann, M.; et al. Reliability of differentiating human coronary plaque morphology using contrast-enhanced multislice spiral computed tomography: A comparison with histology. *J. Comput. Assist. Tomogr.* **2004**, *28*, 449–454. [[CrossRef](#)]
123. Brodoefel, H.; Reimann, A.; Heuschmid, M.; Tsiflikas, I.; Kopp, A.F.; Schroeder, S.; Claussen, C.D.; Clouse, M.E.; Burgstahler, C. Characterization of coronary atherosclerosis by dual-source computed tomography and HU-based color mapping: A pilot study. *Eur. Radiol.* **2008**, *18*, 2466–2474. [[CrossRef](#)]
124. Holzapfel, G.A.; Sommer, G.; Gasser, C.T.; Regitnig, P. Determination of layer-specific mechanical properties of human coronary arteries with nonatherosclerotic intimal thickening and related constitutive modeling. *Am. J. Physiol. Heart Circ. Physiol.* **2005**, *289*, H2048–H2058. [[CrossRef](#)]
125. Pericevic, I.; Lally, C.; Toner, D.; Kelly, D.J. The influence of plaque composition on underlying arterial wall stress during stent expansion: The case for lesion-specific stents. *Med. Eng. Phys.* **2009**, *31*, 428–433. [[CrossRef](#)] [[PubMed](#)]
126. Hajiali, Z.; Dabagh, M.; Debusschere, N.; Beule, M.D.; Jalali, P. Tissue prolapse and stresses in stented coronary arteries: A computer model for multi-layer atherosclerotic plaque. *Comput. Biol. Med.* **2015**, *66*, 39–46. [[CrossRef](#)] [[PubMed](#)]
127. Narayanan, B.; Olender, M.L.; Marlevi, D.; Edelman, E.R.; Nezami, F.R. An inverse method for mechanical characterization of heterogeneous diseased arteries using intravascular imaging. *Sci. Rep.* **2021**, *11*, 22540. [[CrossRef](#)] [[PubMed](#)]
128. Kolluru, C.; Prabhu, D.; Gharaibeh, Y.; Wu, H.; Wilson, D.L. Voxel-based plaque classification in coronary intravascular optical coherence tomography images using decision trees. In *Medical Imaging 2018: Computer-Aided Diagnosis*; SPIE: Bellingham, WA, USA, 2018; Volume 10575, pp. 657–662.
129. Bae, Y.; Kang, S.J.; Kim, G.; Lee, J.G.; Min, H.S.; Cho, H.; Kang, D.Y.; Lee, P.H.; Ahn, J.M.; Park, D.W.; et al. Prediction of coronary thin-cap fibroatheroma by intravascular ultrasound-based machine learning. *Atherosclerosis* **2019**, *288*, 168–174. [[CrossRef](#)]
130. Olender, M.L.; Athanasiou, L.S.; Michalis, L.K.; Fotiadis, D.I.; Edelman, E.R. A Domain Enriched Deep Learning Approach to Classify Atherosclerosis Using Intravascular Ultrasound Imaging. *IEEE J. Sel. Top. Signal Process.* **2020**, *14*, 1210–1220. [[CrossRef](#)]
131. Ciompi, F.; Balocco, S.; Rigla, J.; Carrillo, X.; Mauri, J.; Radeva, P. Computer-aided detection of intracoronary stent in intravascular ultrasound sequences. *Med. Phys.* **2016**, *43*, 5616–5625. [[CrossRef](#)]
132. Zhao, W.; Jenkins, M.W.; Linderman, G.C.; Bezerra, H.G.; Fujino, Y.; Costa, M.A.; Wilson, D.L.; Rollins, A.M. 3-D Stent Detection in Intravascular OCT Using a Bayesian Network and Graph Search. *IEEE Trans. Med. Imaging* **2015**, *34*, 1549–1561.
133. Nishi, T.; Yamashita, R.; Imura, S.; Tateishi, K.; Kitahara, H.; Kobayashi, Y.; Yock, P.G.; Fitzgerald, P.J.; Honda, Y. Deep learning-based intravascular ultrasound segmentation for the assessment of coronary artery disease. *Int. J. Cardiol.* **2021**, *333*, 55–59. [[CrossRef](#)]
134. Shinohara, H.A.-O.; Kodera, S.; Ninomiya, K.A.-O.; Nakamoto, M.; Katsushika, S.A.-O.; Saito, A.; Minatsuki, S.; Kikuchi, H.; Kiyosue, A.; Higashikuni, Y.; et al. Automatic detection of vessel structure by deep learning using intravascular ultrasound images of the coronary arteries. *PLoS ONE* **2021**, *16*, e0255577. [[CrossRef](#)]
135. Macedo, M.M.; Guimarães, W.V.; Galon, M.Z.; Takimura, C.K.; Lemos, P.A.; Gutierrez, M.A. A bifurcation identifier for IV-OCT using orthogonal least squares and supervised machine learning. *Comput. Med. Imaging Graph.* **2015**, *46*, 237–248. [[CrossRef](#)]
136. Gharleghi, R.; Sowmya, A.; Beier, S. Transient wall shear stress estimation in coronary bifurcations using convolutional neural networks. *Comput. Methods Programs Biomed.* **2022**, *225*, 107013. [[CrossRef](#)] [[PubMed](#)]
137. Suk, J.; Haan, P.; Lippe, P.; Brune, C.; Wolterink, J.M. Mesh Convolutional Neural Networks for Wall Shear Stress Estimation in 3D Artery Models. In *Statistical Atlases and Computational Models of the Heart Multi-Disease, Multi-View, and Multi-Center Right Ventricular Segmentation in Cardiac MRI Challenge*; Springer: Cham, Switzerland, 2022; pp. 93–102.
138. Sampedro-Gomez, J.; Dorado-Diaz, P.I.; Vicente-Palacios, V.; Sanchez-Puente, A.; Jimenez-Navarro, M.; San Roman, J.A.; Galindo-Villardón, P.; Sanchez, P.L.; Fernandez-Aviles, F. Machine Learning to Predict Stent Restenosis Based on Daily Demographic, Clinical, and Angiographic Characteristics. *Can. J. Cardiol.* **2020**, *36*, 1624–1632. [[CrossRef](#)]
139. Avram, R.; Olgin, J.E.; Tison, G.H. The Rise of Open-Sourced Machine Learning in Small and Imbalanced Datasets: Predicting In-Stent Restenosis. *Can. J. Cardiol.* **2020**, *36*, 1574–1576. [[CrossRef](#)] [[PubMed](#)]
140. Kushner, F.G.; Hand, M.; Smith, S.C., Jr.; King, S.B., 3rd; Anderson, J.L.; Antman, E.M.; Bailey, S.R.; Bates, E.R.; Blankenship, J.C.; Casey, D.E., Jr.; et al. 2009 Focused Updates: ACC/AHA Guidelines for the Management of Patients With ST-Elevation Myocardial Infarction (updating the 2004 Guideline and 2007 Focused Update) and ACC/AHA/SCAI Guidelines on Percutaneous Coronary Intervention (updating the 2005 Guideline and 2007 Focused Update): A report of the American College of Cardiology Foundation/American Heart Association Task Force on Practice Guidelines. *Circulation* **2009**, *120*, 2271–2306. [[PubMed](#)]
141. Wijns, W.; Kolh, P.; Danchin, N.; Di Mario, C.; Falk, V.; Folliguet, T.; Garg, S.; Huber, K.; James, S.; Knuuti, J.; et al. Guidelines on myocardial revascularization. *Eur. Heart J.* **2010**, *31*, 2501–2555. [[CrossRef](#)] [[PubMed](#)]

142. El-Menyar, A.A.; Al Suwaidi, J.; Holmes, D.R., Jr. Left main coronary artery stenosis: State-of-the-art. *Curr. Probl. Cardiol.* **2007**, *32*, 103–193. [[CrossRef](#)] [[PubMed](#)]
143. Ellwein, L.; Marks, D.S.; Migrino, R.Q.; Foley, W.D.; Sherman, S.; LaDisa, J.F., Jr. Image-based quantification of 3D morphology for bifurcations in the left coronary artery: Application to stent design. *Catheter. Cardiovasc. Interv. Off. J. Soc. Card. Angiogr. Interv.* **2016**, *87*, 1244–1255. [[CrossRef](#)] [[PubMed](#)]
144. Samant, S.; Wu, W.; Zhao, S.; Khan, B.; Sharzehee, M.; Panagopoulos, A.; Makadia, J.; Mickley, T.; Bicek, A.; Boismier, D.; et al. Computational and experimental mechanical performance of a new everolimus-eluting stent purpose-built for left main interventions. *Sci. Rep.* **2021**, *11*, 8728. [[CrossRef](#)] [[PubMed](#)]
145. Chatzizisis Yiannis, S.; Makadia, J.; Zhao, S.; Panagopoulos, A.; Sharzehee, M.; Khan, B.; Samant, S.; Fayaz, M.; Pandya, J.; Akkad, H.; et al. First-in-Human Computational Preprocedural Planning of Left Main Interventions Using a New Everolimus-Eluting Stent. *JACC: Case Rep.* **2022**, *4*, 325–335. [[CrossRef](#)] [[PubMed](#)]
146. Chinnaiyan, K.M.; Akasaka, T.; Amano, T.; Bax, J.J.; Blanke, P.; De Bruyne, B.; Kawasaki, T.; Leipsic, J.; Matsuo, H.; Morino, Y.; et al. Rationale, design and goals of the HeartFlow assessing diagnostic value of non-invasive FFRCT in Coronary Care (ADVANCE) registry. *J. Cardiovasc. Comput. Tomogr.* **2017**, *11*, 62–67. [[CrossRef](#)]
147. Nørgaard, B.L.; Leipsic, J.; Gaur, S.; Seneviratne, S.; Ko, B.S.; Ito, H.; Jensen, J.M.; Mauri, L.; De Bruyne, B.; Bezerra, H.; et al. Diagnostic performance of noninvasive fractional flow reserve derived from coronary computed tomography angiography in suspected coronary artery disease: The NXT trial (Analysis of Coronary Blood Flow Using CT Angiography: Next Steps). *J. Am. Coll. Cardiol.* **2014**, *63*, 1145–1155. [[CrossRef](#)]
148. Ko, B.S.; Cameron, J.D.; Munnur, R.K.; Wong, D.T.L.; Fujisawa, Y.; Sakaguchi, T.; Hirohata, K.; Hislop-Jambrich, J.; Fujimoto, S.; Takamura, K.; et al. Noninvasive CT-Derived FFR Based on Structural and Fluid Analysis: A Comparison With Invasive FFR for Detection of Functionally Significant Stenosis. *JACC Cardiovasc. Imaging* **2017**, *10*, 663–673. [[CrossRef](#)]
149. Kruk, M.; Wardziak, L.; Demkow, M.; Pleban, W.; Pregowski, J.; Dzielinska, Z.; Witulski, M.; Witkowski, A.; Ruzyllo, W.; Kepka, C. Workstation-Based Calculation of CTA-Based FFR for Intermediate Stenosis. *JACC Cardiovasc. Imaging* **2016**, *9*, 690–699. [[CrossRef](#)] [[PubMed](#)]
150. Andreini, D.; Mushtaq, S.; Pontone, G.; Rogers, C.; Pepi, M.; Bartorelli, A.L. Severe in-stent restenosis missed by coronary CT angiography and accurately detected with FFRCT. *Int. J. Cardiovasc. Imaging* **2017**, *33*, 119–120. [[CrossRef](#)] [[PubMed](#)]
151. Zun, P.S.; Narracott, A.J.; Chiastra, C.; Gunn, J.; Hoekstra, A.G. Location-specific comparison between a 3D in-stent restenosis model and micro-CT and histology data from porcine in vivo experiments. *Cardiovasc. Eng. Tech.* **2019**, *10*, 568–582. [[CrossRef](#)]
152. Corti, A.; Colombo, M.; Migliavacca, F.; Rodriguez Matas, J.F.; Casarin, S.; Chiastra, C. Multiscale computational modeling of vascular adaptation: A systems biology approach using agent-based models. *Front. Bioeng. Biotechnol.* **2021**, *9*, 744560. [[CrossRef](#)]
153. Hwang, M.; Garbey, M.; Berceci, S.A.; Tran-Son-Tay, R. Rule-based simulation of multi-cellular biological systems—a review of modeling techniques. *Cell Mol. Bioeng.* **2009**, *2*, 285–294. [[CrossRef](#)] [[PubMed](#)]
154. Boyle, C.J.; Lennon, A.B.; Prendergast, P.J. In silico prediction of the mechanobiological response of arterial tissue: Application to angioplasty and stenting. *J. Biomech. Eng.* **2011**, *133*, 081001. [[CrossRef](#)]
155. Zahedmanesh, H.; Van Oosterwyck, H.; Lally, C. A multi-scale mechanobiological model of in-stent restenosis: Deciphering the role of matrix metalloproteinase and extracellular matrix changes. *Comput. Methods Biomech. Biomed. Eng.* **2014**, *17*, 813–828. [[CrossRef](#)] [[PubMed](#)]
156. Caiazzo, A.; Evans, D.; Falcone, J.-L.; Hegewald, J.; Lorenz, E.; Stahl, B.; Wang, D.; Bernsdorf, J.; Chopard, B.; Gunn, J.; et al. A Complex Automata approach for in-stent restenosis: Two-dimensional multiscale modelling and simulations. *J. Comput. Sci.* **2011**, *2*, 9–17. [[CrossRef](#)]
157. Nolan, D.R.; Lally, C. An investigation of damage mechanisms in mechanobiological models of in-stent restenosis. *J. Comput. Sci.* **2018**, *24*, 132–142. [[CrossRef](#)]
158. Corti, A.; Colombo, M.; Rozowsky, J.M.; Casarin, S.; He, Y.; Carbonaro, D.; Migliavacca, F.; Rodriguez Matas, J.F.; Berceci, S.A.; Chiastra, C. A predictive multiscale model of in-stent restenosis in femoral arteries: Linking haemodynamics and gene expression with an agent-based model of cellular dynamics. *J. R. Soc. Interface* **2022**, *19*, 20210871. [[CrossRef](#)]
159. Razavi, A.; Sachdeva, S.; Frommelt, P.C.; LaDisa, J.F., Jr. Patient-Specific Numerical Analysis of Coronary Flow in Children With Intramural Anomalous Aortic Origin of Coronary Arteries. *Semin. Thorac. Cardiovasc. Surg.* **2021**, *33*, 155–167. [[CrossRef](#)] [[PubMed](#)]
160. Razavi, A.; Sachdeva, S.; Frommelt, P.C.; LaDisa, J.F. Computational Assessment of Hemodynamic Significance in Patients With Intramural Anomalous Aortic Origin of the Coronary Artery Using Virtually Derived Fractional Flow Reserve and Downstream Microvascular Resistance. *J. Biomech. Eng.* **2022**, *144*, 031005. [[CrossRef](#)] [[PubMed](#)]
161. Ghorbanniahassankiadeh, A.; Marks, D.S.; LaDisa, J.F. Correlation of computational instantaneous wave-free ratio with fractional flow reserve for intermediate multivessel coronary disease. *J. Biomech. Eng.* **2021**, *143*, 051011. [[CrossRef](#)]